ELUCIDATING COMPLEX CHARGE DENSITY WAVE STRUCTURES IN LOW-DIMENSIONAL MATERIALS BY SCANNING TUNNELING MICROSCOPY

HONGJIE DAI, JIE LIU AND CHARLES M. LIEBER

Department of Chemistry and Division of Applied Sciences, Harvard University, Cambridge, MA 02138, USA.

1. Applications Of Scanning Probe Microscopy

An important goal of condensed matter research is to understand how microscopic or atomic level structural and electronic characteristics of a solid determine observable properties like superconductivity and magnetism. This goal is motivated by the recognition that such an understanding will enable scientists ultimately to design rationally bulk solids and nanostructures having predictable properties. Instrumental methodologies that provide a real-space picture of the connectivity of atoms in a solid and/or the local electronic structure are perhaps most appealing since they can probe materials directly in the space (real vs. reciprocal) that we often think, and can directly characterize defects and disorder that play significant roles in determining the properties of solids. Furthermore, real-space probes are required to assess the intrinsic structural and electronic properties of very small material structures that are a focus of the burgeoning area of nanotechnology.

In the past decade, scanning probe microscopies (SPMs), such as scanning tunneling microscopy (STM) and atomic force microscopy (AFM), have rapidly grown into uniquely powerful tools for probing microscopic properties of materials [1-23]. STM can be used to probe the surface structure and electronic states of conducting and semiconducting materials directly on the atomic scale [1-15], while AFM can be used to assess the structure and elastic properties of insulators, semiconductors and conductors at the nanometer scale [16-26]. SPMs are also effective tools for manipulating matter on the atomic to nanometer scales, constructing individual nanostructures, and probing the properties of individual nanostructures [11,26-30].

SPMs are by their very nature highly surface sensitive techniques. The ability to probe the uppermost layers of a material is an important advantage in studies of very small supported structures, such as nanocrystals on surfaces, and in fundamental investigations of growth and catalysis on metal and semiconductor surfaces [31-34]. Surface sensitivity can, however, be a severe limitation in studies designed to probe the bulk properties of a material since the coordinatively

F. W. Boswell and J.C. Bennett (eds.),
Advances in the Crystallographic and Microstructural Analysis of Charge Density Wave Modulated Crystals, 225–257.

unsaturated surface atoms of three-dimensional (3D) solids typically adopt a different geometrical arrangement (i.e., reconstruct) from those in the bulk. However, highly anisotropic materials--- for example, layered solids possessing strong covalent bonding in two-dimensional (2D) sheets with weak noncovalent bonds holding these layers together--- cleave preferentially along planes defined by the weak noncovalent bonds. The coordination of atoms at the surface cleavage plane in such a low-dimensional solid is similar to that in the bulk (i.e., the covalent bonding is unchanged), and thus these surfaces do not reconstruct. SPM studies of such low-dimensional materials offer the opportunity to probe atomic level structural and electronic properties that are representative of the bulk of a material.

Low-dimensional solids also offer a great richness and complexity of physical phenomena that make them generally an important focal point of condensed matter research. For example, many two-dimensional and one-dimensional metal chalcogenide materials are known to exhibit complex charge density wave (CDW) and spin density wave phases [35], and furthermore it is well-known that the layered structure of the copper oxide superconductors is central to the high-temperature superconductivity that these materials exhibit [36]. STM has been extremely effective in elucidating, not only the atomic structures of these fascinating materials, but also collective phenomena such as the pinning of CDW and magnetic vortex lattices [10-15,37-39]. In the case of charge density wave systems, STM can provide detailed structural information about the atomic lattice and the electron density modulation with a resolution of ~1 Å. Detailed real-space STM pictures also provide an unambiguous approach to understanding complex CDW structures that have been long-standing and controversial problems unanswered by diffraction.

In this chapter, we present recent advances in probing and understanding the microscopic structures of charge density wave phases in low dimensional metal chalcogenide compounds obtained using the STM approach. The scope of the chapter is as follows: first, we will describe the STM technique; then we will review applications of STM to elucidating the low temperature CDW phases in the one-dimensional $NbSe_3$ system and further in the 2D 1T-TaS_2 system. Next, we will focus on incommensurate CDW structures in chemically impurity doped 1T-TaS_2 materials, and the wealth of physics revealed by real-space studies. Finally, we will conclude with a look at future directions such as CDWs in very small 2D nanocrystals.

2. Background: Scanning Tunneling Microscopy

In this section, the instrumentation and theoretical concepts that are essential for understanding STM studies will be discussed. More detailed reviews can be found elsewhere [1,2,6-9,40,41]. A typical microscope is illustrated schematically in Figure 1. The underlying basis for the operation of the microscope is electron tunneling between a sharp metal tip and a conducting sample. When the tip and sample are brought sufficiently close, their wave functions can overlap. If a bias voltage V is then applied to the sample, a tunneling current I will flow between the sample and tip. Electrons will tunnel from filled electronic states in the tip to empty states in the sample when V is positive, and

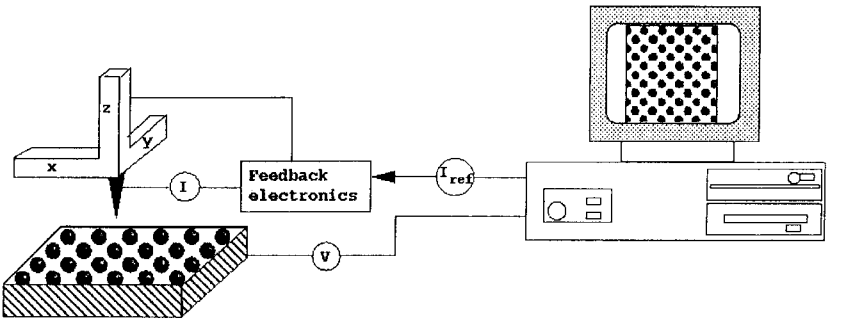

Fig. 1. Schematic view of a tunneling microscope.

conversely, electrons will tunnel from filled sample states to empty tip states when V is negative. The tunneling current that flows when V is applied varies exponentially with the tip-sample separation, and for a typical work function of 4 eV, I decreases 10-fold for an angstrom increase in separation. The strong exponential dependence of the tunneling current on distance enables STM to achieve high vertical resolution. An atomic resolution map of the surface can then be generated by rastering the tip over the sample with angstrom level control using piezoceramic positioners. Experimental images are typically acquired in the constant current mode in which a feedback loop controls the vertical position of the tip above the sample so that I is equal to a reference current (I_{ref}) at all coordinates on the surface. Features in constant current mode images thus correspond to vertical-displacements of the positioner needed to maintain a constant tunneling current.

Essential to the interpretation of such STM data is an understanding of the response of the tunneling current to the barrier properties, applied voltage, etc.; insight into these problems can be obtained from analyses of the tunneling problem [42-46]. As first discussed by Tersoff and Hamann, an expression for I can be readily derived by assuming noninteracting sample and tip wave functions, and then using perturbation theory [42]. In the limit of small bias voltage and low temperature this treatment yields

$$I = (2\pi/\hbar)e^2V\Sigma|M_{st}|^2\delta(E_s-E_f)\delta(E_t-E_f) \quad (1)$$

where M_{st} is the tunneling matrix element between wave functions on the tip, ψ_t, and sample, ψ_s. As shown by Bardeen [47], the tunneling matrix element can be written as

$$M_{st} = (\hbar^2/2m)\int(\Psi_t^*\nabla\Psi_s - \Psi_s\nabla\Psi_t^*)dS \quad (2)$$

where the integral corresponds to a surface within the barrier region between the sample and tip. To evaluate M_{st} in a way that the resulting expression for I can be compared quantitatively to STM images in general (i.e., not for one specific choice of sample and tip) requires several approximations. Tersoff and Hamann showed that by assuming the tip forms a locally spherical

potential well with only s-wave functions, I could be expressed as

$$I \propto \Sigma_s |\Psi_s(r_o)|^2 \delta(E_s - E_f) \quad (3)$$

By definition the summation is the local density of sample electronic states, $\rho(r_o,E)$, at the center of curvature of the tip

$$\rho(r_o,E) \equiv \Sigma_s |\Psi_s(r_o)|^2 \delta(E_s - E_f) \quad (4)$$

Thus, constant current images correspond to contours of constant density of sample electronic states. Because a CDW causes a variation of the electronic states close to the E_f, STM represents a uniquely sensitive and direct probe of the structure and amplitude of the CDW lattice. In the next section, we review recent STM studies in pure materials and give some background information about CDWs.

3. Charge Density Waves In Pure Materials

3.1 THE ONE-DIMENSIONAL $NbSe_3$ SYSTEM

A large number of quasi-one-dimensional materials exhibit CDW transitions including $NbSe_3$, TaS_3, $(TaSe_4)_2I$, $K_{0.3}MoO_3$ and organic conductors such as $(fluoranthene)_2PF_6$ and $(perylene)_2Au(maleonitriledithiolate)_2$ [48-51]. Among them the two most widely studied materials are $NbSe_3$ and $K_{0.3}MoO_3$ [51-53]. In this section, we will focus on $NbSe_3$. $NbSe_3$ crystals are built up from a Se trigonal prismatic cage surrounding a metallic Nb chain. The $NbSe_6$ trigonal prisms are stacked on top of each other to form linear chains along the **b**-axis of a monoclinic unit cell (Figure 2a). In $NbSe_3$, the crystal lattice unit cell (a_0 = 10.0 Å, b_0 = 3.5 Å, c_0 = 15.6 Å) [52] contains three pairs of trigonal chains labeled as types I, II, and III (Figure 2b). These three chains exhibit distinct CDW states [53]. Two independent charge density wave transitions are observed in $NbSe_3$ with transition temperatures of 144 K and 59 K. These transitions were first observed as DC resistivity anomalies in the transport studies by Monceau et al. in the 70's [52]. Subsequent X-ray diffraction and transport studies by Fleming et al. proved the existence of two independent CDWs and showed that these have wave vectors of (0.00, 0.243, 0.00) and (0.5, 0.263, 0.5) at 144 K and 59 K respectively. Hence, both of these CDWs are incommensurate with respect to the atomic lattice; the incommensurability is maintained down to 4.2 K [54].

In the past two decades, $NbSe_3$ has been a model system for experimental condensed matter studies of collective sliding, non-linear phenomena and pinning [49,50,55-59]. The detailed CDW structure has been studied by a variety of techniques including X-ray diffraction [54,60,61], NMR [62] and scanning tunneling microscopy [63]. Synchrotron-radiation X-ray diffraction and NMR studies have found that the 144 K and 59 K CDW modulations are primarily associated with atomic displacements of the type III and type I chains, respectively. These observations are consistent with electronic structure calculations that suggest the type-II chains are not involved in CDW formation [53].

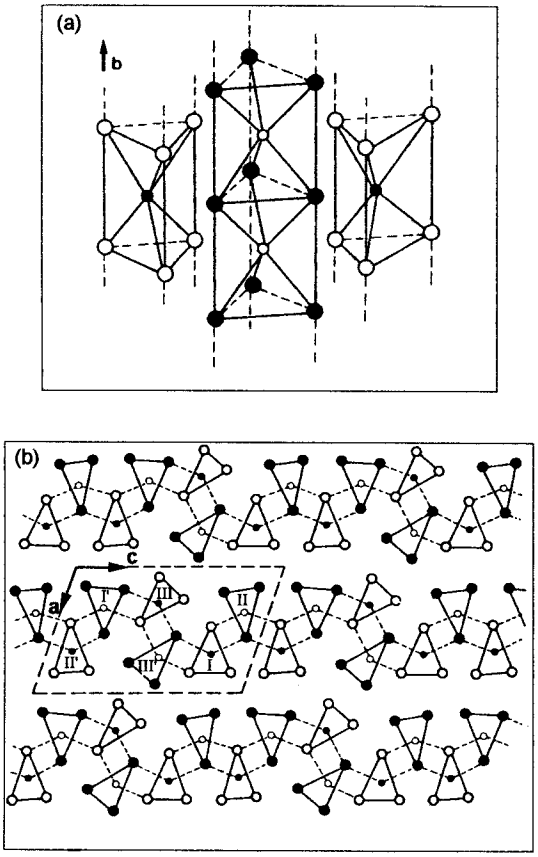

Fig. 2. (a) $NbSe_3$ chains running along the **b** axis; (b) The structure of $NbSe_3$ projected along [0 1 0].

High resolution low-temperature STM studies of $NbSe_3$ by Coleman and coworkers were also used to probe the complex CDW states in real space [63]. Shown in Figure 3 is an STM image of the b-c plane of $NbSe_3$ acquired at 4.2 K by Coleman et al. [63]. In contrast to synchrotron X-ray diffraction and NMR studies, CDWs were observed on all three types of chains. Comparison of these 4.2 K images with STM images acquired at 77 K [64-66] led the authors to conclude that the 59 K CDW forms on type I and II chains, while at 144 K a CDW forms on the type III chain. Furthermore, it can be seen that the type I and II chains of adjacent unit cells exhibit CDW modulations that are out of phase by 180°, meaning that the CDW maxima matches the CDW minima on adjacent type I or II chains. The type I and II chains are therefore associated with the low temperature CDW state and have a wavelength of $2c_0$. The CDW on type III chains is found to be in phase in adjacent unit cells, and the repeat distance on each chain is ~$4b_0$; these results are consistent with diffraction data for the high temperature CDW. Besides providing detailed phase information of the complex CDW in $NbSe_3$, the STM data also showed that the amplitude of CDW modulation on type III chains is large, while the CDW amplitude on type I and II chains is relatively weak.

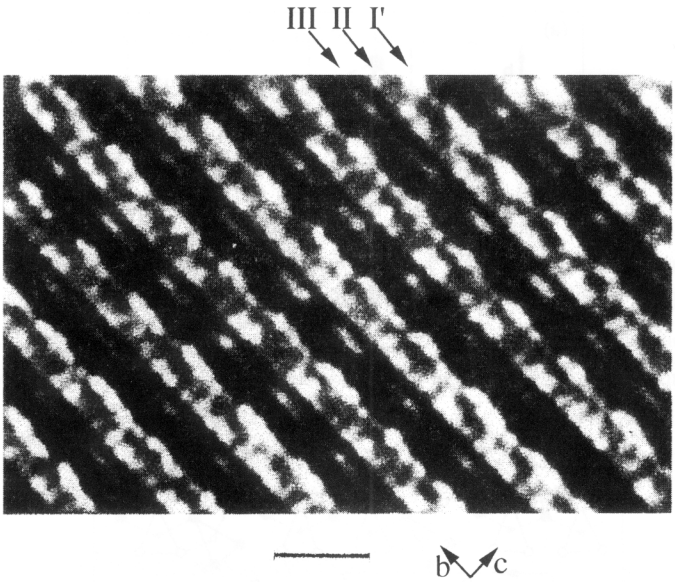

Fig. 3. STM image of charge density waves in $NbSe_3$ at 4.2 K. Reproduced from Ref. 63.

The STM results of Coleman et al. suggest that all three types of chains in $NbSe_3$ are conducting and contribute to the Fermi surface sections that are responsible for the CDW formation. These results contradict models [53] and other experiments [60-62] suggesting that the type II chains are nearly insulating and are excluded from CDW formation. As described in another chapter of this book, this conflict was considered by Whangbo [67] and coworkers using electronic band structures calculations and numerical simulation of resulting STM images. This latter work suggests that the character of electrons at the Fermi level is dominated by Nb atoms on type I and III chains. However, due to geometric reasons, STM only detects Se atoms. Their calculations showed that these Se atoms make similar contribution to the LDOS for all type I, II and III chains. Thus, this analysis supports the STM studies of Coleman. These results demonstrate that real space STM imaging and analysis can provide new insight about complex CDW structures that are otherwise difficult to observe and enable a deeper understanding of the electronic structures of one dimensional materials.

3.2 TWO-DIMENSIONAL METAL DICHALCOGENIDES: 1T-TaS_2

The dichalcogenides of the group IV, V, and VI transition metals have layered structures in which the transition metal (M) occupies either octahedral or trigonal prismatic sites between two layers of hexagonally close packed chalcogenide atoms (X) (Figure 4) [68,69]. In general, the MX_2 compounds are quasi-2D materials since the X-M-X layers are held together by strong covalent-ionic bonding, whereas the interactions holding adjacent layers together are much weaker dispersion forces. These materials cleave readily between the weakly bonded layers to yield free surfaces that

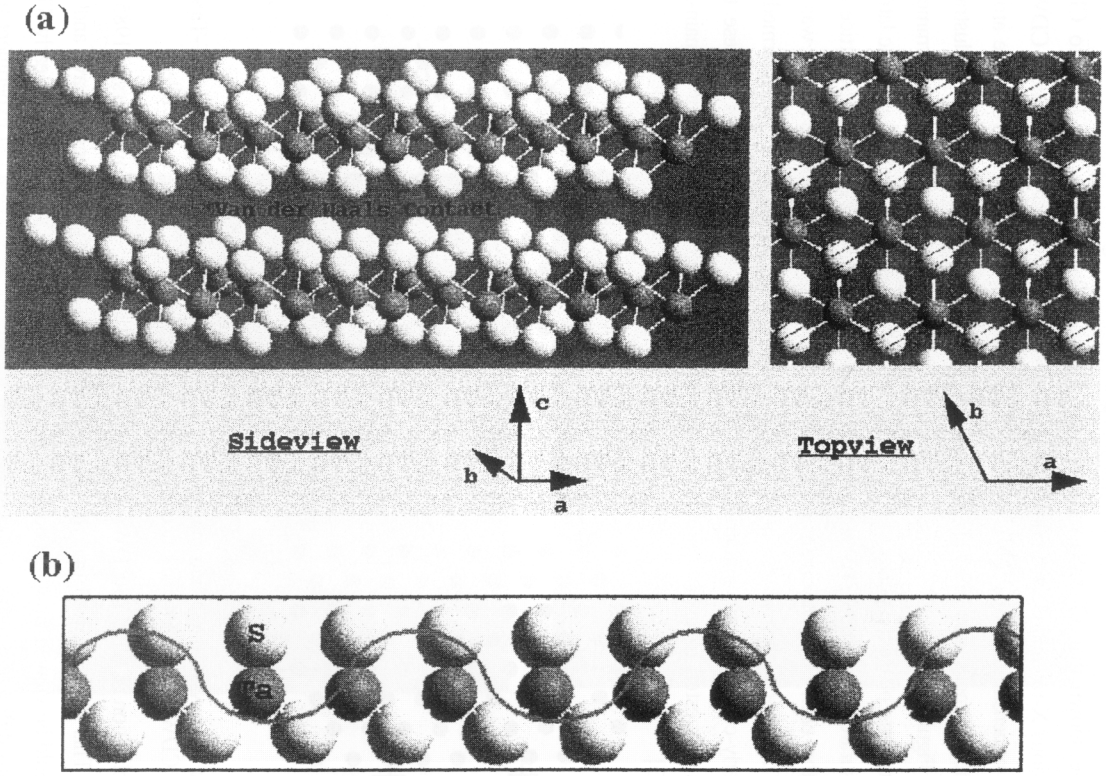

Fig. 4. (a) Schematic view of two M-X-M layers of MX_2 (e.g., M=Ta, X=S) that are bonded primarily via dispersion forces. The sulfur atoms are arranged in hexagonal close packed planes. (b) One-dimensional view of a sinusoidal CDW in a single M-X-M layer.

are structurally and electronically similar to the bulk [68-71].

Among the MX_2 compounds, 1T-TaS_2 exhibits one of the most complex and interesting CDW phase diagrams. At high temperatures the compound 1T-TaS_2 is metallic; however, on cooling below 543 K 1T-TaS_2 exhibits four distinct temperature dependent CDW states [69,70]. A schematic of the CDW and atomic lattice in 1T-TaS_2 is shown in Figure 4b. Electronic structure calculations have shown that 1T-TaS_2 exhibits large Fermi surface nesting that leads to CDW formation. Previous X-ray and electron diffraction have showed that the high temperature CDW in 1T-TaS_2 is incommensurate, while for $T < 183$ K the CDW rotates 13.9^o relative to the atomic lattice to become commensurate [69-71]. The real-space structures of these phases are illustrated schematically in Figure 5. The CDW superlattice of both phases has a regular hexagonal symmetry. In the incommensurate phase the peaks of CDW are located randomly relative to the atomic lattice. In the commensurate phase, the CDW superlattice rotates 13.9^o relative to the atomic lattice and expands 2% so that each CDW maxima is oriented over an equivalent atomic lattice site. It was not possible using diffraction techniques, however, to resolve the structures of the intermediate temperature nearly-commensurate and triclinic nearly commensurate CDW phases. These two phase had been suggested to exhibit either uniformly incommensurate structures or domain-like structures [72,73].

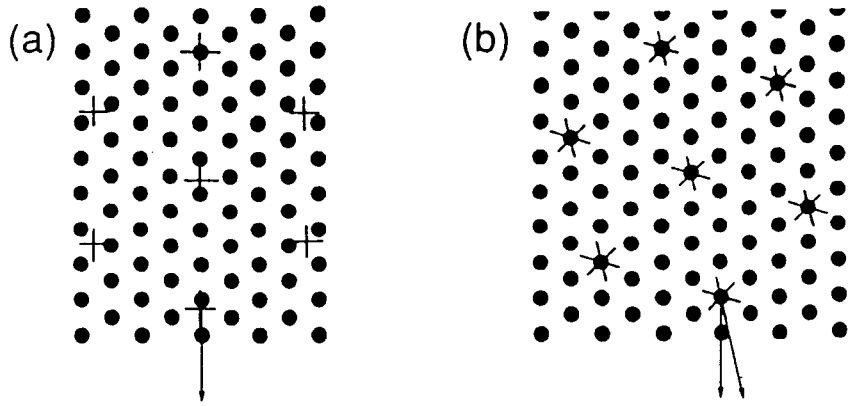

Fig. 5. Schematic topviews of the (a) incommensurate and (b) commensurate CDW phases in 1T-TaS_2. The CDW maxima are indicated by the crosses and the atomic lattice by the filled.

The first application of STM to CDWs was carried out by Coleman and coworkers in 1985 on 1T-TaS_2 [74]. This work showed that the charge modulation of a charge density wave and the atomic lattice could be viewed simultaneously in real space. In addition, comparison of early STM data with previous diffraction results demonstrated that the surface sensitive STM experiment truly reflected the bulk properties of 1T-TaS_2 [10,74]. The ability of STM to determine simultaneously both CDW and atomic lattice positions has subsequently been exploited by our group and others to resolve the complicated structural details of the intermediate temperature CDW phases in TaS_2 that previously could not be determined by diffraction techniques [64,75-78].

STM studies of the real-space structure of 1T-TaS_2 at room temperature showed that the nearly-commensurate CDW phase adopts a novel, hexagonal, domain-like structure, in which there is a periodic variation in the CDW amplitude that occurs on a wavelength much larger than the CDW wavelength, λ (Figure 6) [75]. In large area images, the CDW maxima (Figure 6a, filled white circles) define a regular hexagonal superlattice with average wavelength in agreement with

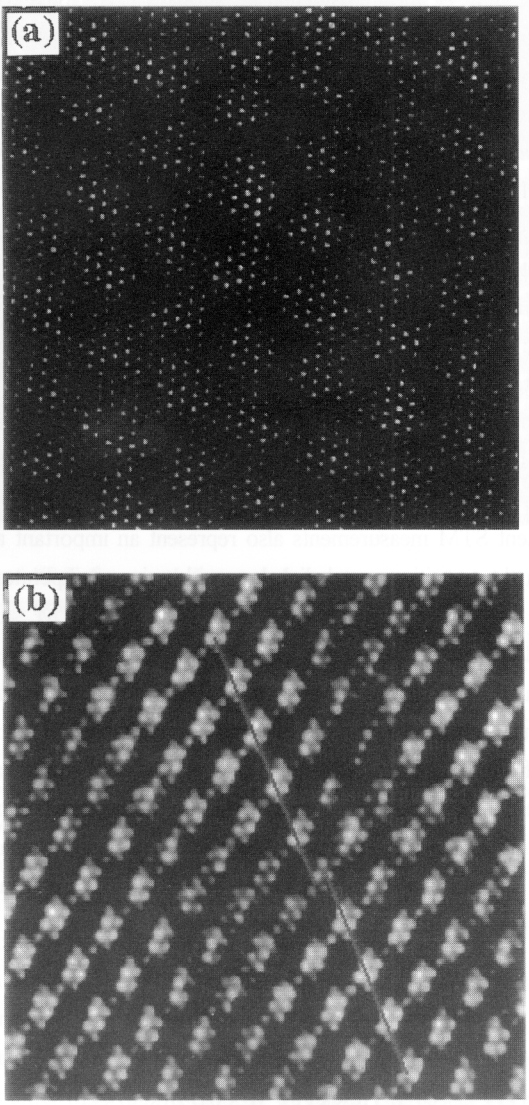

Fig. 6. Room temperature STM images of 1T-TaS_2. (a) 50 x 50 nm^2 image showing CDW maxima and domains. (b) Atomic-resolution image of four domains. The domains are highlighted by circular white lines. The white lines indicate the single atom phase shift that occurs between the CDWs in adjacent domains. Reproduced from Ref. 75.

diffraction and STM measurements. The amplitude of the CDW maxima further exhibits a larger periodic modulation that defines domains consisting of relatively high-amplitude CDW maxima separated by lower amplitude domain boundaries. The roughly circular, high amplitude domains are arranged in a hexagonal superstructure with a period of approximately 70 Å at room temperature. Hence, the nearly commensurate CDW exhibits a fascinating hierarchy of structures: the hexagonal atomic lattice with period 3.35 Å, the fundamental hexagonal CDW lattice with period of ~12 Å, and the hexagonal domain superlattice with period 70 Å.

Atomic resolution images of the nearly commensurate phase have provided further insight into the complex structure of the domain phase (Figure 6b). First, these images show that there are well-defined phase shifts of one atomic lattice period between the CDWs in adjacent domains [75,76]. The abrupt changes in CDW phase are clear in real-space images, but are quite difficult to detect in diffraction measurements. Secondly, the high-resolution images show that there is a similar arrangement of atoms at each CDW maxima within a domain, thus indicating that the CDW is approximately commensurate (e.g., see schematic in Figure 5) in the domains. Because the actual angle between the atomic lattice and CDW superlattice can be measured, such images also afford the ability to address quantitatively the issue of commensurability. Significantly, these measurements showed the angle within single domains was that expected for a commensurate CDW, ~13.9°. Taken together, these STM studies unambiguously resolved the long standing controversy about the structure of the nearly commensurate CDW phase in 1T-TaS_2.

Temperature-dependent STM measurements also represent an important approach for further probing CDW phases in the transition metal dichalcogenides since temperature variations can be used to assess melting and other phase transitions [10,76,77]. STM studies of the nearly commensurate phase in 1T-TaS_2 first demonstrated the power of such measurements [76]. Images recorded between 200 and 350 K show the hexagonal CDW domain structure described above. The period of the domain structure was found to undergo a remarkable and unexpected change with temperature decreasing from 100 Å at 200 K to ~60 Å at 350 K (Figures 7a-c). At still higher temperatures, there is an abrupt loss of the domain structure as the true incommensurate phase is formed (Figure 7d). Significantly, the decrease in domain size appears similar to a second-order melting transition as the sample temperature is raised, however, it is important to point out this corresponds to melting of an electronic (CDW) lattice and not the atomic lattice.

4. Charge Density Wave Pinning

4.1 INTRODUCTION TO CHARGE DENSITY WAVE PINNING

An important goal in condensed matter research is to understand the factors that determine the structure, electronic properties and phase transitions in materials since such knowledge will lead the way to the rational design of new solids with predictable properties [79,80]. Essential to the

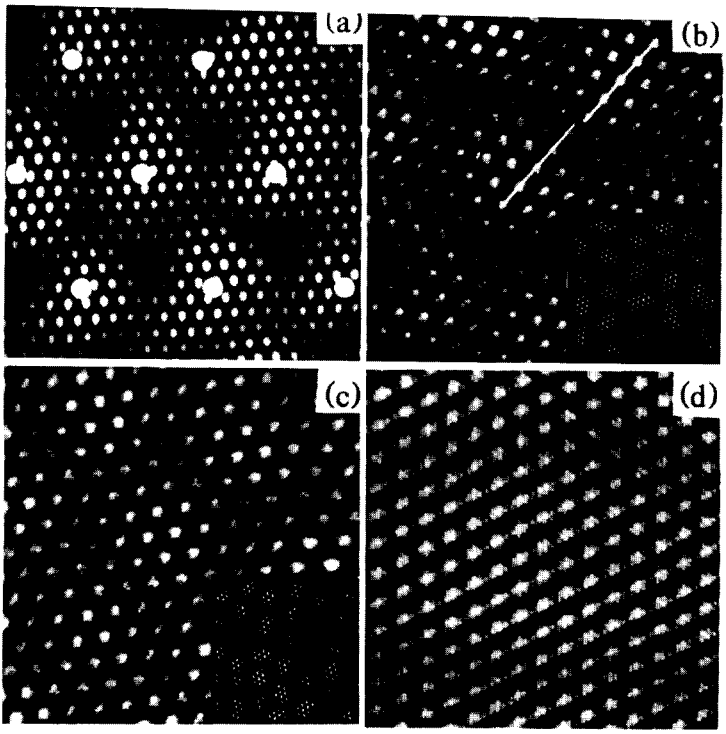

Fig. 7. STM images of 1T-TaS_2 recorded at sample temperatures of (a) 242, (b) 298, (c) 349, and (d) 357 K. The images are (a) 30 x 30, (b) 17.5 x 17.5, and (c), (d) 15.5 x15.5 nm^2 in size. The insets in (b) and (c) are 30 x 30 nm^2. The domain center positions for an ideal hexagonal structure are marked with white dots in (a). Reproduced from Ref. 76.

achievement of this goal is a detailed understanding of how material properties vary and can be controlled by atomic level modifications such as substitutional doping. In principle, doping is a straight-forward process with readily predictable effects (e.g., doping semiconductors). However, in many materials, especially those that exhibit cooperative phenomena such as charge density waves and superconductivity, the role of dopants and impurities is not well understood [13,81]. Past difficulties in elucidating the microscopic effects of dopants and impurities on material properties can be traced to the fact that conventional diffraction and spectroscopic techniques provide only an averaged view of a solid [82]. These techniques have not been able to assess unambiguously structural disorder and electronic inhomogeneity in doped solids [13,81,83].

Impurities in charge density wave compounds tend to interact or pin CDWs because their electronic properties differ from the host atoms. It can be envisioned that an impurity in the atomic lattice will attract or repel a CDW maxima, and thus distort the otherwise perfect CDW lattice. However, this qualitative picture encounters much complication due to factors such as the strength of the interaction or pinning, the randomness and concentration of impurities, and the susceptibility (or rigidity) of CDWs to distortion. Previous diffraction studies have found that in metal-doped

TaS_2 compounds, the CDW diffraction peaks became progressively broader as dopant concentration is increased [69,71]. These results provided the first structural evidence of CDW pinning by metal dopant atoms, and showed that pinning can distort the overall CDW structure. Nevertheless, a detailed picture of CDW pinning on a microscopic scale was inaccessible from diffraction studies, and thus comparison with theoretical models on structural effects of CDW pinning was not possible.

In the following section, we will focus on STM studies of the Nb-doped 1T-TaS_2 system to illustrate the effects of pinning by random impurities in a CDW system. We will first discuss CDW pinning in the framework of a theoretical model, and then present STM images of the pinned CDW state. Systematic structural analyses and calculations will be presented and compared with theoretical models. We will show that a deeper understanding not only of charge density waves, but also of complex yet generic phenomena in two-dimensional systems such as collective pinning, dislocation related hexatic ordering and two-dimensional melting can be obtained using this approach.

4.2 THEORY OF CHARGE DENSITY WAVE PINNING

The one-dimensional Fukuyama-Lee-Rice (FLR) CDW pinning model [84,85] has been the starting point for many studies of CDW-impurity pinning. In the FLR model the electron density distribution $\rho(\mathbf{r})$ is treated as a sinusoidal wave with a constant amplitude ρ_0 modulated over a uniform background electron density ρ_{av}:

$$\rho(\mathbf{r}) = \rho_{av} + \rho_0 \cos(\mathbf{Q} \cdot \mathbf{r} + \phi(\mathbf{r})) \tag{5}$$

The wave vector of the CDW is $\mathbf{Q} = 2\mathbf{k}_f$ and the real-space periodicity of the electron density is π/k_f. The FLR model treats the impurity-CDW interaction within a Ginzburg-Landau framework, where the order parameter is the CDW phase, $\phi(\mathbf{r})$. For a perfect CDW free of impurities, $\phi(\mathbf{r})$ is a constant. Interestingly, if $\phi(\mathbf{r})$ is constant and if the wave vector $\mathbf{Q}$ is incommensurate with the atomic lattice, then the energy of the CDW state is independent of its position relative to the atomic lattice [86].

However, $\phi(\mathbf{r})$ may vary with position when impurities are introduced into the host atomic lattice since impurities can pin the CDW phase. To calculate the expected behavior of the CDW in presence of impurities we consider several limiting cases for a one-dimensional system. In the commensurate state ($\mathbf{Q} = 2\pi/n\mathbf{a}$) the CDW is in registry with the atomic lattice and is thus strongly pinned to the atomic lattice. Impurity pinning does not perturb significantly the commensurate CDW state [87]. On the other hand, an incommensurate CDW ($\mathbf{Q} \neq 2\pi/n\mathbf{a}$) interacts weakly with the underlying lattice. Variations in the lattice potential due to impurity atoms can thus effectively distort or pin an incommensurate CDW. Qualitatively, an attractive pinning potential will distort CDW maxima towards the nearest impurities to minimize the energy. The interaction of the impurities with the incommensurate CDW is examined below.

First, we assume that each impurity has a short-ranged pinning potential and that this potential has the same magnitude for every impurity. The total pinning potential distribution is thus a function of the positions of the randomly quenched impurities:

$$V_{pin}(\mathbf{r}) = V_0 \Sigma_i \delta(\mathbf{r} - \mathbf{R}_i) \tag{6}$$

where R_i is the i^{th} impurity position vector and the sum is over all impurities.

Similar to other solids, the CDW lattice has rigidity that can be quantified by the elastic constant $\kappa \approx h v_f / A_0$, where A_0 is the unit cell area [88]. Because a distortion of the CDW lattice from equilibrium will cost the system elastic energy, it is necessary to account for both pinning and CDW rigidity simultaneously. This is accomplished by computing the potential energy gain associated with pinning and the elastic energy loss due to CDW distortions using the following effective Hamiltonian:

$$H = \int \rho(\mathbf{r}) V_{pin}(\mathbf{r}) d^d\mathbf{r} + \frac{\kappa}{2} \int [\nabla \phi(\mathbf{r})]^2 d^d\mathbf{r} \tag{7}$$

The first term is the pinning energy, the second term is the elastic energy and d is the dimensionality of the system. Combining equations (5), (6) and (7) yields

$$H = \rho_0 V_0 \Sigma_i \cos(\mathbf{Q} \cdot \mathbf{R}_i + \phi(\mathbf{R}_i)) + \frac{\kappa}{2} \int [\nabla \phi(\mathbf{r})]^2 d^d\mathbf{r} \tag{8}$$

The pinning energy depends on the random impurity configuration, and the elastic energy depends on the CDW phase fluctuations caused by pinning.

The phase variation is determined by minimizing the total energy. Two limiting cases, strong and weak pinning, are considered. In the strong pinning regime, the elastic energy is much less than the pinning potential. Hence, the CDW phase is pinned to each impurity site with the phase given by $\mathbf{QR}_i + \phi(\mathbf{R}_i) = -\pi$ (Figure 8). The energy determined for the limiting case of strong pinning is then $-\rho_0 |V_0| N_i$, where N_i is the total number of impurities; that is, the energy is simply proportional to the number of impurities. On the other hand, in the weak pinning regime the pinning energy is much smaller than the energy required to deform the CDW. Hence, phase distortions do not occur at each impurity site [$\mathbf{QR}_i + \phi(\mathbf{R}_i) \neq -\pi$], but rather, $\phi(\mathbf{r})$ varies on a length scale much larger than the impurity spacing (Figure 8). Since each term in the sum in equation 8 can be either positive or negative the total pinning energy grows only as $N_i^{1/2}$ (vs. N_i for strong pinning). An interesting consequence of the FLR weak pinning model is that the CDW will be unstable to domain formation for $d < 4$. These domains should consist of distinct regions containing many impurities within which the CDW phase varies smoothly. The STM studies described below provide a unique test of this prediction.

Quantitatively, a parameter ε is used to characterize the pinning strength and separate the strong and weak pinning regimes:

$$\varepsilon = \frac{\rho_0 V_0}{\kappa n_i^{2/d-1}} \tag{9}$$

where $\rho_0 V_0$ is the pinning potential energy per impurity and $\kappa \cdot n_i^{2/d-1}$ is the dimensionality

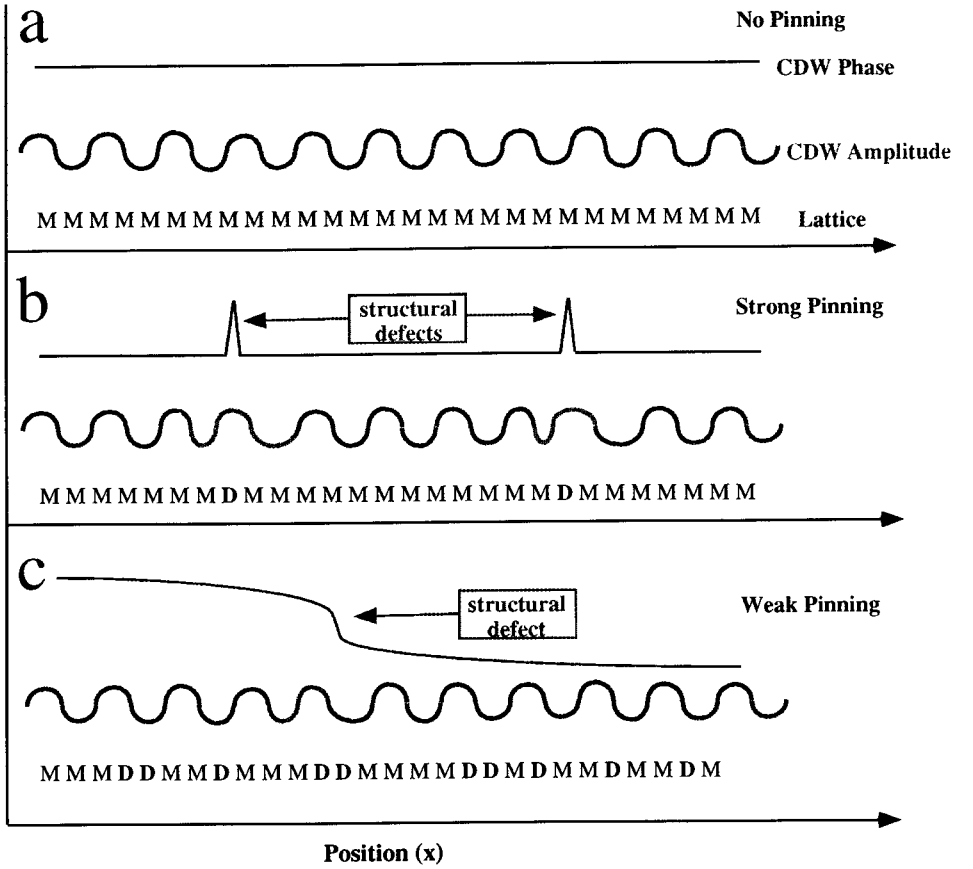

Fig. 8. Plots of the CDW phase, $\phi(r)$, and amplitude versus position for (a) a perfect one-dimensional lattice and (b, c) for lattices that contain impurities, D. The abrupt variation in $\phi(r)$ at each impurity site (b) corresponds to strong pinning. The smooth variation in $\phi(r)$ over a distance containing several impurities (c) corresponds to weak pinning.

dependent elastic energy per impurity [88]. Hence, $\varepsilon >> 1$ corresponds to the strong pinning regime and $\varepsilon << 1$ corresponds to the weak pinning regime.

As indicated above, approximately constant phase domains containing many impurities are expected in the weakly pinning regime. The length scale of these domains can be estimated using scaling arguments of Imry and Ma [89]. Specifically, they showed that the pinning energy scales as $L^{d/2}$ while the elastic energy scales as L^{d-2}. Hence, the pinning energy gain is $\rho_o V_o N_i^{1/2} = \rho_o V_o n_i^{1/2} L^{d/2}$, and the elastic energy cost is κL^{d-2} (assume $\phi(\mathbf{r})$ varies by $\sim \pi$ over length L). We can thus define a critical length L_c, which defines the average size of constant phase domains, by minimizing the energy with respect to L:

$$L_c = \alpha \cdot \frac{1}{\varepsilon} \cdot d_i, \tag{10}$$

where α is of order unity and $d_i = n_i^{-1/d}$ is the average impurity spacing.

Specific defects in the CDW lattice arising from CDW-impurity pinning have also been studied theoretically. For example, McMillan showed that the energy cost for a single dislocation diverges logarithmically with the size of the sample [87]; this behavior is similar to that of a dislocation in an ordinary solid. The existence of dislocations can be explained using the scaling argument outlined above. First, a dislocation loop with size L will contain $n_i L^d$ impurities. The pinning energy gain is $\sim \rho_o V_o n_i^{1/2} L^{d/2}$ and the elastic energy cost for creating the dislocation is $\sim \kappa$ up to a logarithm [87,90]. Since the total energy is the same as in the treatment of domains we can obtain the critical length given by equation 10. In the case of dislocations, L_c is comparable to the average separation between dislocation.

Lastly, it is important to point out that the FLR model only considers phase fluctuations of the CDW; amplitude fluctuations of the CDW are ignored. A justification for ignoring amplitude fluctuations is that the energy cost for an amplitude fluctuation is significantly higher than that of the long wavelength phase fluctuations treated by FLR. Recent work by Coppersmith shows, however, that amplitude fluctuations do have nontrivial effects on the CDW state [91]. Hence, we believe that the relative importance of phase and amplitude fluctuations is an area that requires additional theoretical and experimental study.

4.3 RESULTS OF CHARGE DENSITY WAVE PINNING IN $Nb_xTa_{1-x}S_2$

4.3.1 STM Images

Here we review studies of niobium-substituted tantalum disulfide, $Nb_xTa_{1-x}S_2$. Substitution of isoelectronic Nb(IV) for Ta(IV) represents the weakest perturbation on the potential that is possible with metal substitution, and thus serves as the best test of the weak pinning regime [15,92,93]. The effect of Nb-substitution on the macroscopic transport properties of these $Nb_xTa_{1-x}S_2$ materials have been assessed by variable-temperature resistivity measurements (Figure 9). In general, it is well-established [13,69,70] that Nb-substitution (and other metal substitutions) decreases the transition temperature from the high-temperature incommensurate (IC) CDW state to the lower temperature nearly-commensurate state. Qualitatively, the suppression in the transition temperature can be rationalized by assuming that the IC state is stabilized by impurity pinning. Macroscopic measurements do not, however, address the fundamental details of pinning that were outlined above. To develop a microscopic understanding of the CDW-impurity interaction we turn to STM studies of the CDW state in these materials.

High resolution STM images of the $Nb_xTa_{1-x}S_2$ materials are shown in Figures 10-12. Images of the IC CDW phase of undoped TaS_2 samples [92,93] exhibit a well-ordered hexagonal structure. In contrast, substitution of Nb causes disorder in the IC CDW lattice (Figures 10-12). The images of the Nb-doped materials exhibit areas in which the CDW lattice has hexagonal order and regions containing defects. These defects introduce disorder into the CDW lattice. The predominant defects observed in the x(Nb) < 0.07 samples are dislocations. Dislocations are formed by the

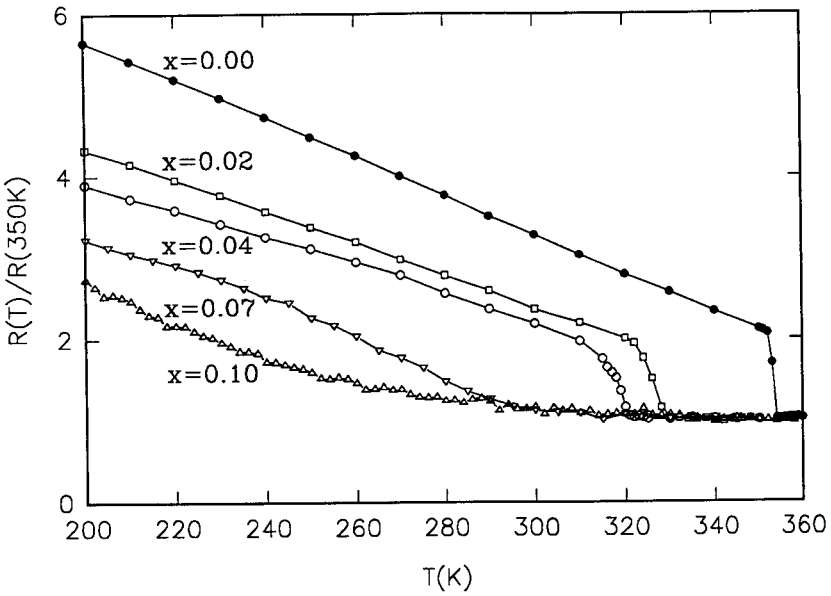

Fig. 9. Normalized resistance versus temperature curves recorded on the $Nb_xTa_{1-x}S_2$ materials. Reproduced from Ref. 15.

insertion of extra half rows of CDW sites in the lattice; black lines in Figure 10a highlight the creation of two dislocations in a x(Nb) = 0.02 sample. Importantly, there is a significant strain field associated with the dislocations [90]. The CDW can relax the strain field by locally deforming through site positional shifts and rotations (Figure 10a), although these deformations introduce disorder into the lattice. We have also found one or more CDW site vacancies close to the dislocation core in many of the images (Figure 10b). This latter observation is interesting since it is completely analogous to the classical behavior of vacancies and dislocations in the atomic lattice of materials [90]. Since STM can be used to study directly such defects we believe that it will be interesting in the future to explore the generality of the $M_xTa_{1-x}S_2$ materials as models for the behavior of crystal defects and the dynamics of vacancy/dislocation formation.

As the impurity concentration increases to x(Nb) = 0.04 a higher density of defects (predominantly dislocations) is observed in the CDW lattice (Figure 11). The CDW rows near the dislocations are distorted as discussed above. However, in areas free of dislocations the CDW lattice is locally ordered. We have highlighted several dislocation cores by constructing Burgers loops (Figure 11). The Burgers loop consists of an equal number of steps along each lattice direction; the loop will remain open if it encloses a single dislocation. The vector pointing from start to end of the loop, the Burgers vector, uniquely defines the dislocation [90]. We find that the Burgers vectors defining the CDW dislocations in the Nb-doped samples occur along each of the three crystallographic axes, and thus it is apparent that impurity-induced dislocations occur randomly in the CDW lattice. In the samples containing higher impurity concentrations, x(Nb) = 0.07 and 0.10 the STM images exhibit extended defects (Figure 12). The CDW lattice in these latter samples

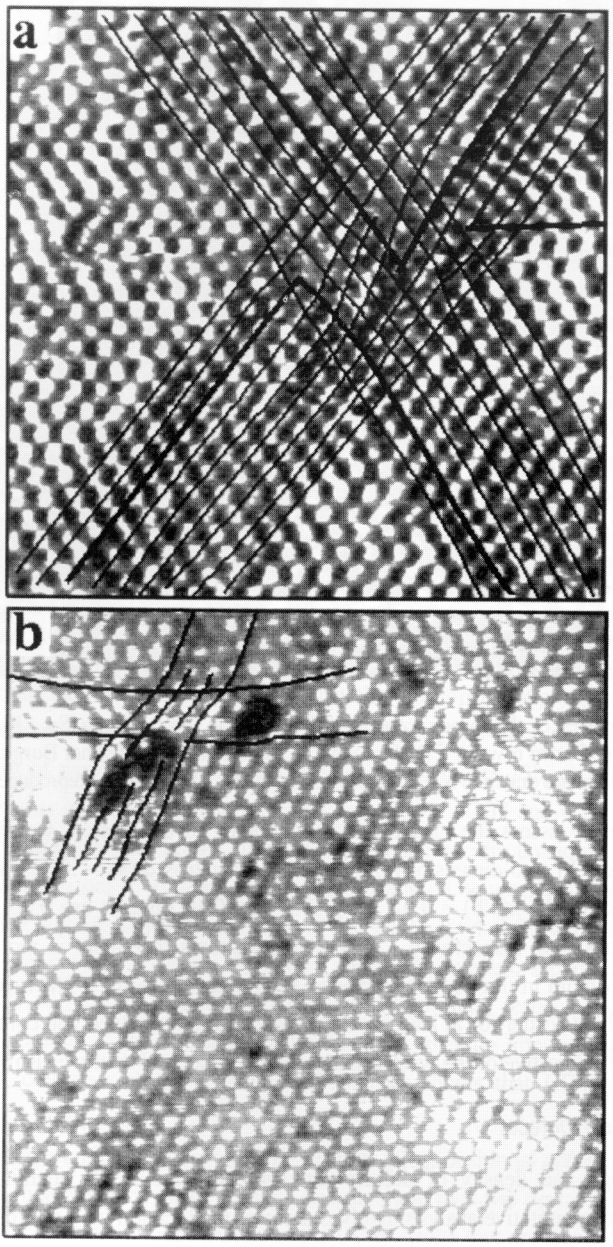

Fig. 10. STM images of the incommensurate CDW state in $Nb_{0.02}Ta_{0.98}S_2$. Black lines highlight the insertion of an extra row of CDW maxima. The extra rows in (a) are highlighted with heavy black lines. Vacancies are also seen in (b). Reproduced from Ref. 92.

exhibits significant disorder with regions of hexagonal order and positional order extending only several lattice constants.

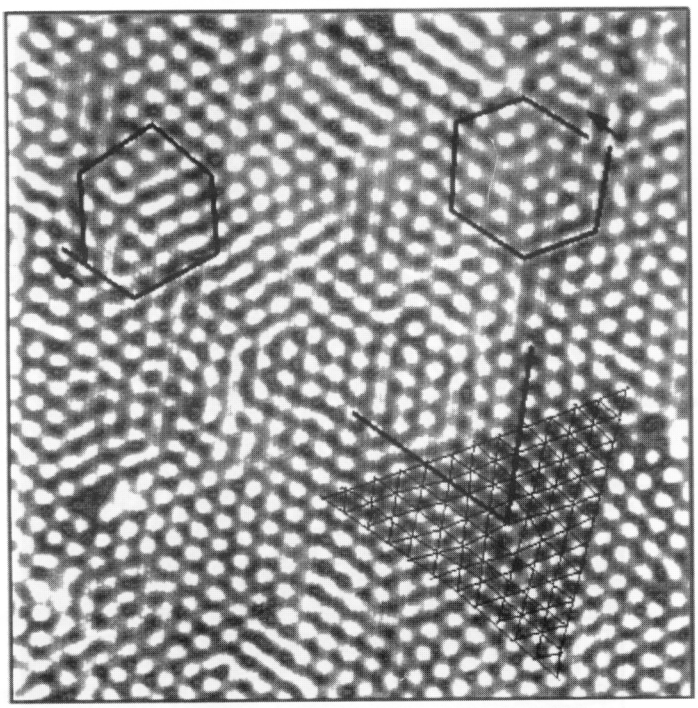

Fig. 11. STM images of the incommensurate CDW state in $Nb_{0.04}Ta_{0.96}S_2$. Black lines highlight the insertion of extra rows of CDW maxima in the lattice. Two distinct Burgers loops and Burgers vectors are drawn to highlight dislocations in the CDW lattice. Reproduced from Ref. 92.

To qualitatively assess the nature of CDW pinning in this system we first calculate the Nb impurity spacing. In two-dimensions the impurity spacing is $d_i(x) = n_i^{-1/2}$, and thus the average impurity spacing for the x(Nb) = 0.02, 0.04, 0.07 and 0.10 samples are 0.80, 0.57, 0.43 and 0.36 CDW lattice constants, respectively. This estimate shows that there is more than one impurity atom/CDW maximum in the doped samples investigated. Since the STM images indicate that the CDW lattice exhibits order for at least several lattice constants (which will contain many impurities) these results are suggestive of the weak pinning regime described by the FLR model.

4.3.2 Topological Defects

The topology and density of defects can also be assessed by quantitative image analysis [15,93-96]. The quantitative analysis involves defining the location (x, y coordinates) of each CDW maximum and the unique nearest neighbors in the lattice. Once the lattice points are determined, a sweep-line algorithm [97] is used to construct the Voronoi diagram for the lattice. The Voronoi diagram uniquely defines the nearest neighbors of all lattice points [98]. To illustrate defects in the lattice we triangulate the Voronoi diagram by drawing "bonds" from all CDW lattice points to their nearest neighbors. This resulting plot is termed the Delauney triangulation diagram. In our CDW system fully coordinated lattice sites are indicated by six bonds, while defects contain a smaller or

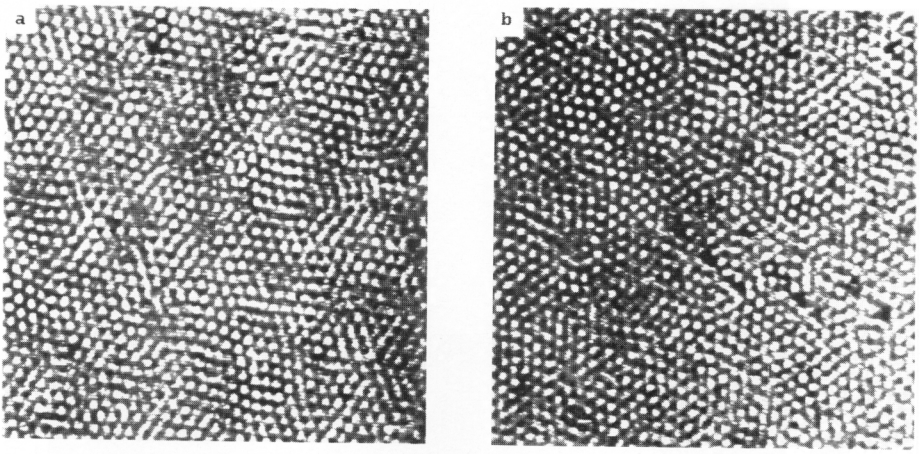

Fig. 12. STM images of the incommensurate CDW phase in (a) $Nb_{0.07}Ta_{0.93}S_2$ and (b) $Nb_{0.1}Ta_{0.9}S_2$. Reproduced from Ref. 92.

greater number of bonds. Typical results obtained from the analysis of x(Nb) = 0, 0.02, 0.04, 0.07 and 0.10 samples are shown in Figure 13. In these triangulation diagrams we have highlighted the defect sites by shading. Inspection of images recorded on pure TaS_2 samples show that the CDW lattice is free of topological defects; that is, all of the lattice sites are six-fold coordinated (Figure 13a). The triangulations explicitly show, however, that the Nb-doped materials have topological defects in the CDW lattice. At low concentrations of impurities, x(Nb) = 0.02 and 0.04, we find that the dislocations consist of five-fold/seven-fold disclination pairs (Figures 13b, c). Extended defect networks are also obvious in the triangulation data for the x(Nb) = 0.07 and 0.10 samples. These extended topological defects consist of dislocations, vacancies and free disclinations.

This data has also been used to evaluate the average separation between dislocations. We find that the average spacing between dislocations in the x(Nb) = 0.02, 0.04, 0.07 and 0.1 samples is 12, 8, 5, and 3 lattice constants, respectively. As stated above, the average separation between Nb impurity atoms is 0.80, 0.57, 0.43 and 0.26 CDW lattice constants, respectively. The average spacing between dislocations is thus always greater than the average impurity spacing; that is, impurity pinning is a collective effect. Hence, this analysis shows that CDW pinning in the $Nb_xTa_{1-x}S_2$ materials is weak.

The topological defects highlighted in Figure 13 strongly affect positional order. For example, a dislocation displaces lattice points by about a lattice constant, and thus will destroy positional order on a scale of the size of dislocation loop. Areas of the CDW lattice that are free from dislocations should, however, exhibit a smooth variation in the CDW phase; i.e., the domains in the FLR model. In Figure 14 we show a typical large scale image with several phase coherent regions highlighted to demonstrate this important point. This image also shows clearly that the local crystallographic axes of adjacent domains are rotated with respect to one another.

Further analysis of large area images containing different impurity concentrations shows that the

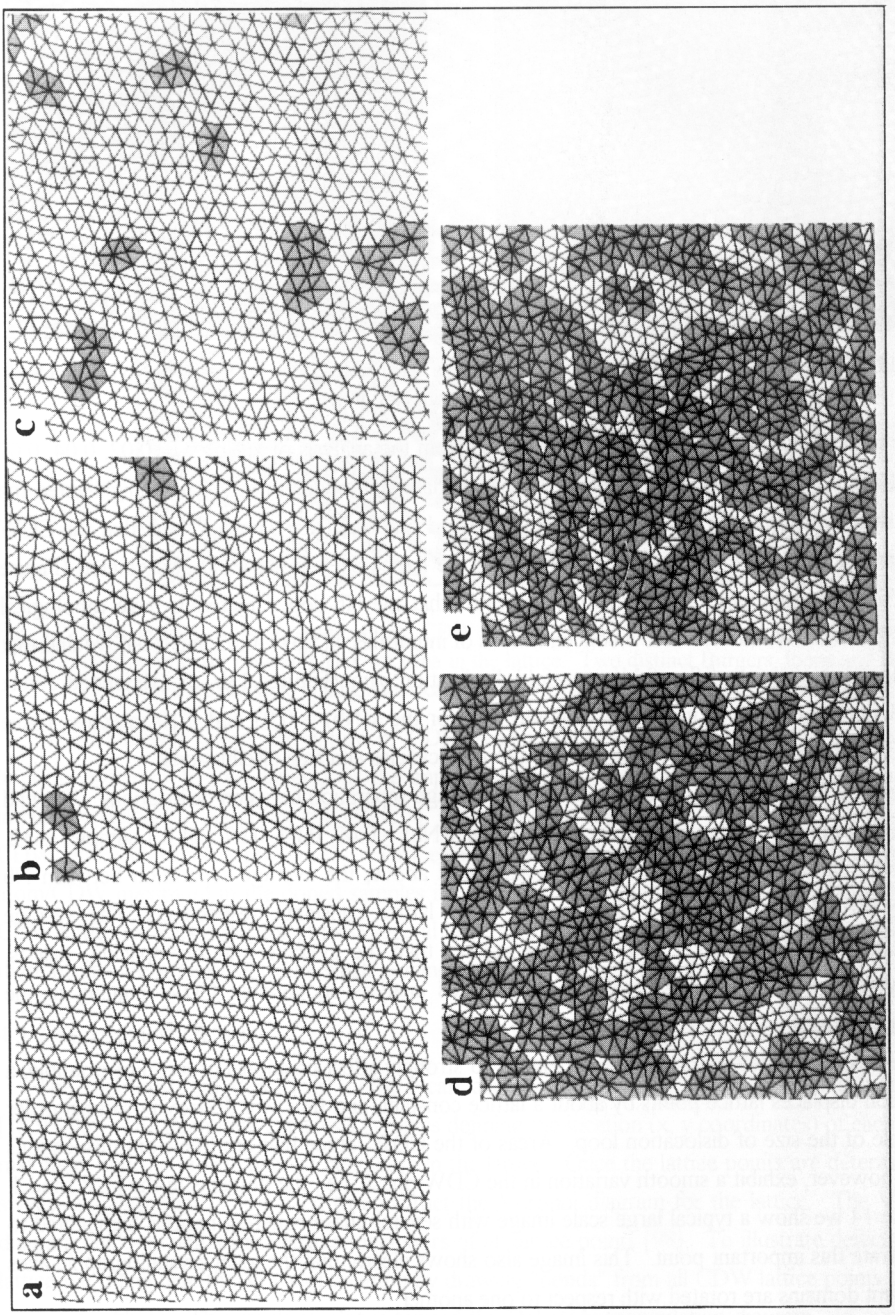

Fig. 13. Delauney triangulations of the STM images recorded on $Nb_xTa_{1-x}S_2$ crystals where (a), (b), (c), (d) and (e) correspond to $x = 0, 0.02, 0.04, 0.07$ and 0.10, respectively. Lattice sites that do not have six fold coordination are highlighted by shading. Reproduced from Ref. 93.

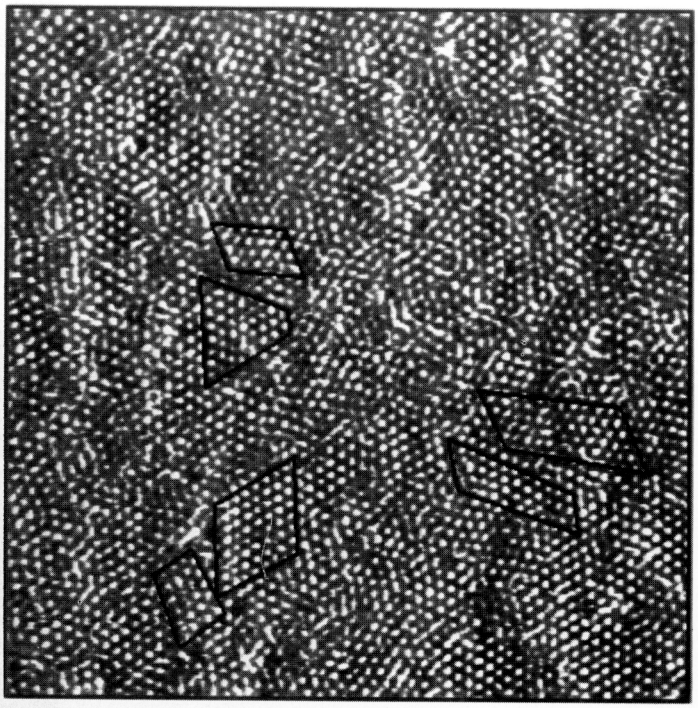

Fig. 14. A large area STM image of the incommensurate CDW lattice of a $Nb_{0.07}Ta_{0.93}S_2$ sample. Several adjacent domains containing positionally ordered lattices are highlighted with black lines. Note that adjacent domains are rotated with respect to each other. Reproduced from Ref. 92.

area of the ordered regions (the domain size) shrinks as the impurity concentration increases. This behavior follows directly from equation 10. Importantly, if we take the dislocation separation as the critical length, L_c, and using the impurity spacing d_i given above, we find that the calculated value of the FLR pinning parameter ε is ~ 0.1. These results quantitatively confirm that the system is in the weakly pinned regime.

4.3.3 Two-Dimensional Order

Above we have characterized the nature of CDW pinning and defects. More generally, it is important to examine the consequences of the disorder produced by weak pinning since this phenomena is important to a number of important physical systems [95,96]. To quantify disorder, we first examine the structure factor $S(\mathbf{k})$.

$$S(\mathbf{k}) = |\rho(\mathbf{k})|^2 \tag{11}$$

where $\rho(\mathbf{k}) = \int \rho(\mathbf{r}) e^{i\mathbf{k}\cdot\mathbf{r}} d\mathbf{r}$ is the Fourier transform of the number density of lattice points. $S(\mathbf{k})$ provides an average of the structural effects of pinning. The results for the Nb-substituted materials are shown in Figure 15. $S(\mathbf{k})$ for pure TaS_2 (not shown) exhibit sharp six-fold symmetric peaks (Bragg peaks). These peaks broaden both radially and angularly as the impurity concentration

increases to 0.04. For the x(Nb) = 0.07 and 0.10 the first order Bragg peaks have broadened to form a ring whose intensity has a six fold modulation. The angular broadening is due to CDW rotations that were discussed above. This broadening indicates a loss of orientational order; however, it is not possible to provide a quantitative measure of the orientational disorder from this S(**k**) data. In addition, the radial widths of the Bragg peaks indicate that the translational correlation length is short in all of the Nb-doped materials. Notably, our S(**k**) data are qualitatively similar to the results expected for second order melting transition in 2D [92-94,96,99,100].

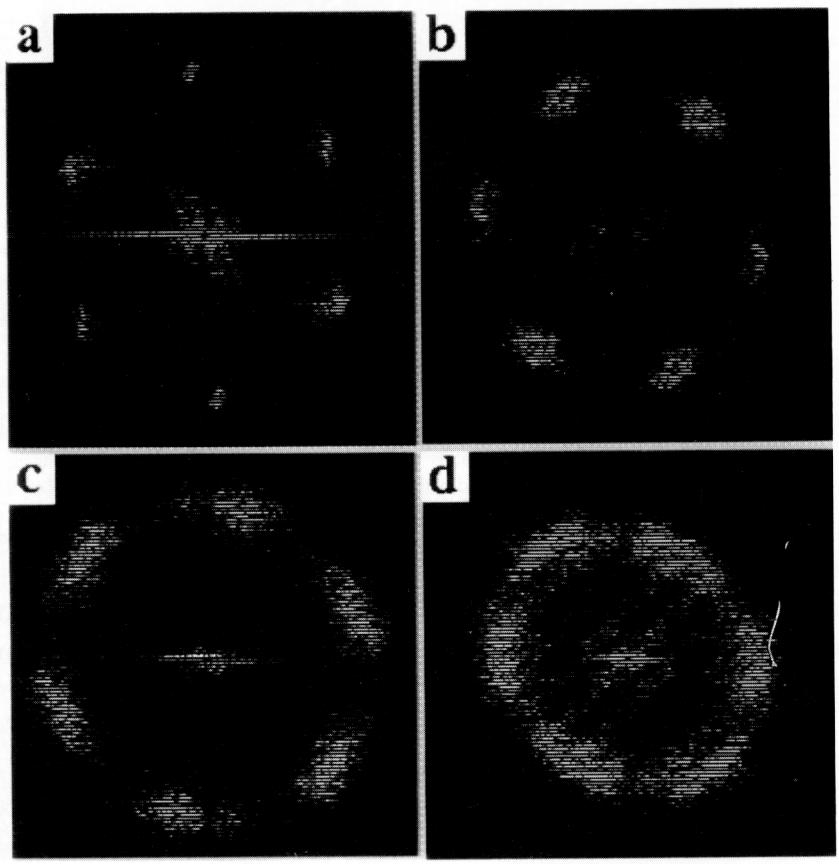

Fig. 15. Structure factors corresponding to the CDW lattices of (a) x = 0.02, (b) x = 0.04, (c) x = 0.07, and (d) x = 0.10 $Nb_xTa_{1-x}S_2$ materials. Reproduced from Ref. 15.

To provide a more quantitative measure of the order in this system and how it is affected by impurity pinning we have investigated systematically the radial distribution, translational correlation and orientational correlation functions. The radial distribution function is defined as $g(r) = \langle n(r) \rangle / n_0$, where n(r) is the point density at a distance r from the origin of the structure and n_0 is the average density of points. For a general structure, g(r) tends to 1 as r goes to infinity; that is, the distribution of lattice points at large distances appears uniform. Plots of g(r) determined from

STM images of the $Nb_xTa_{1-x}S_2$ materials are presented in Figure 16. For the pure sample, g(r) oscillates strongly out to more than 10 lattice constants. The persistent oscillation indicates that positional order is long range. When the impurity level increases to 0.02 and 0.04 the amplitude of the oscillations in g(r) decreases and the oscillations die out much more rapidly than in g(r) for the pure material (Figures 16a-c). For the x(Nb) = 0.07 or 0.10 materials the amplitude of the peaks in g(r) is further reduced and those peaks only persist to the second or third nearest neighbors. These results indicate that Nb impurity pinning induced disorder destroys translational order in this CDW system.

The order of the CDW system can be further characterized by calculating the translational and orientational correlation functions. These functions were first introduced by Mermin [101] in his theoretical studies of the positional and orientational order of 2D solids. In two dimensions, the translational correlation function is defined as

$$G_T(\mathbf{r}) = \langle \psi(\mathbf{0})\psi(\mathbf{r})^* \rangle \tag{12}$$

where

$$\psi(\mathbf{r}) = \frac{1}{3}\sum_{i=1}^{3} e^{\,i\mathbf{G}_i\cdot\mathbf{r}} \tag{12a}$$

is the translational order parameter for a hexagonal lattice at position r. This order parameter consists of the local Fourier components of the number density of lattice points at reciprocal lattice vectors G. The translational correlation function is equivalent to the Debye-Waller factor and its Fourier transform gives the structure factor $S(\mathbf{k})$. Thus, it measures how lattice points are correlated positionally in real space.

The orientational correlation function for a 2D lattice with hexagonal symmetry is defined as

$$G_6(\mathbf{r}) = \langle \psi_6(\mathbf{0})\psi_6(\mathbf{r})^* \rangle, \tag{13}$$

where

$$\psi_6(\mathbf{r}) = \sum_{i=1}^{nn} e^{\,i6\theta_i(\mathbf{r})} \tag{13a}$$

is the orientational order parameter at position $\mathbf{r}$. $\theta(\mathbf{r})$ is the local bond angle with respect to a given direction. Bonds correspond to the lines that connect the nearest neighbors (nn) defined by the Voronoi analysis and Delauney triangulation discussed earlier. The sum is over all nn bonds of a point at position $\mathbf{r}$. This definition for the orientational correlation function is also valid for liquids since the average coordination number of a 2D liquid is also six.

It is instructive to examine the general behavior of these correlation functions before we proceed with the analysis of the CDW system. First, translational and orientational order of a crystal lattice are often coupled to one another. For example, a grain boundary rotates the area (volume) of one part of a crystal lattice relative to an adjacent one; this rotation disrupts both translational and orientational order. However, it is also possible for $G_T(r)$ and $G_6(r)$ to exhibit very different dependencies with r. First, theoretical studies have shown that long wavelength phonon fluctuations destroy only translational order in a 2D solid; orientational order will remain long-range [101,102].

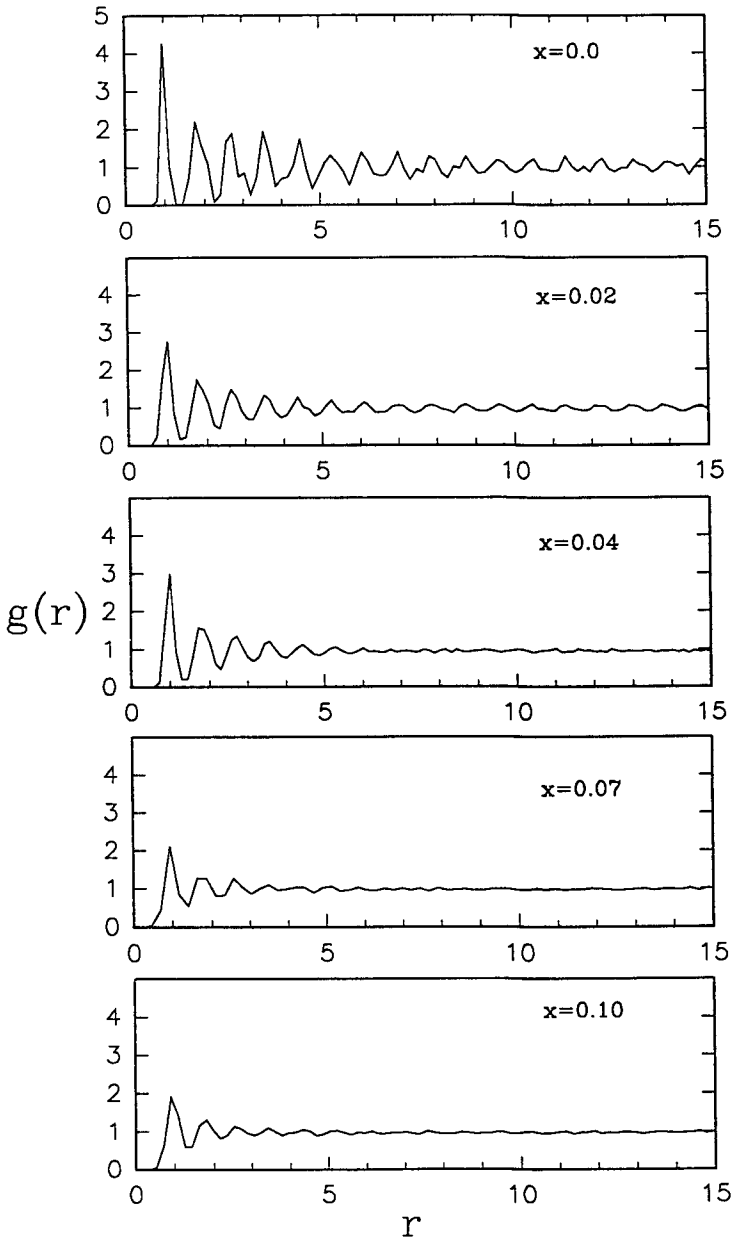

Fig. 16. Radial distribution functions for the $Nb_xTa_{1-x}S_2$ materials. The x-axis corresponds to CDW lattice constants. Reproduced from Ref. 93.

Secondly, Halperin and Nelson [103,104] have shown that dislocations affect translational and orientational order differently in 2D crystals: translational order is destroyed and decays exponentially, while orientational order is quasi long-ranged and decays algebraically.

Calculated results for $G_T(\mathbf{r})$ and $G_6(\mathbf{r})$ for the $Nb_xTa_{1-x}S_2$ materials are shown in Figure 17. $G_T(\mathbf{r})$ and $G_6(\mathbf{r})$ decay very slowly over 20 lattice constants for the incommensurate CDW lattice of the pure sample. This quasi long-range order is indicative of a crystalline state. In contrast, all of the samples that contain Nb impurities exhibit a rapid decay of translational order. This decay in $G_T(\mathbf{r})$ can be fit reasonably well to an exponential of the form $G_T(\mathbf{r}) = \exp(-r/\xi_T)$ where ξ_T is the translational correlation length. The ξ_T's are 7-10, 3-6, 2-3, 1-2 CDW lattice constants for the x(Nb) = 0.02, 0.04, 0.07 and 0.10 samples, respectively. These results demonstrate quantitatively that the dislocations and other defects arising from weak pinning destroy translational order. In contrast, we find that the orientational order decays slowly for the x(Nb) = 0.02 and 0.04 samples, although $G_6(\mathbf{r})$ decays rapidly for x(Nb) = 0.07 and 0.10 (Figure 17). If the x(Nb) = 0.02, 0.04, 0.07, and 0.10 $G_6(\mathbf{r})$ data are fit with an exponential, $G_6(\mathbf{r}) = \exp(-r/\xi_6)$, we obtain orientational correlation lengths (ξ_6) of 200, 100, 11 and 5 lattice constants, respectively. A better fit to $G_6(\mathbf{r})$ for x(Nb) = 0.02 and 0.04 is obtained, however, using an algebraic decay, $G_6(\mathbf{r}) = r^{-\eta}$, with η = 0.03 and 0.12, respectively.

The simultaneous observation of long-range orientational order and short range translational order in the x(Nb) = 0.02 and 0.04 samples is strongly suggestive of the hexatic state that was proposed on the basis of theoretical studies of 2D melting driven by topological defects [103,104]. This theory predicts that 2D melting involves two continuous phase transitions. First, a crystalline solid phase that has quasi long range translational order and long range orientational order ($G_T(\mathbf{r}) = r^{-\xi}$; $G_6(\mathbf{r}) \sim 1$) undergoes a second order transition to the hexatic phase that has short range translational order and quasi long range orientational order: $G_T(\mathbf{r}) = \exp(-r/\xi_T)$; $G_6(\mathbf{r}) = r^{-\eta}$. At higher temperature, the hexatic undergoes a second continuous transition to a liquid phase that has short range translational and orientational order: $G_T(\mathbf{r}) = \exp(-r/\xi_T)$; $G_6(\mathbf{r}) = \exp(-r/\xi_6)$. The results for the CDW phase in $Nb_xTa_{1-x}S_2$ show similar behavior, and thus we suggest that the CDW lattice evolves from crystalline (x = 0) through hexatic glass (x = 0.02 - 0.04) to liquid-like (x > 0.07) states. We assign the intermediate state to a hexatic glass (versus equilibrium hexatic) since the impurity distribution in these materials is quenched. The fundamental difference between the 2D melting theory and our study is that the topological defects arise from thermal fluctuations in the former and from pinning to a quenched impurity distribution in our work. Since statistical averaging differs for equilibrium versus quenched disorder [105], we have compared further the CDW system to equilibrium melting.

First, we can estimate the power law exponent η using the relationship $\eta = 9c/\pi$, where c is a fractional area of dislocation cores, derived for dislocations in thermal equilibrium [94]. The values of η calculated in this way, 0.02 and 0.13, are in excellent agreement with the values obtained from fits to $G_6(\mathbf{r})$ for x(Nb) = 0.02 and 0.04. This agreement suggests that dislocations arising from impurity pinning are responsible for the decay in orientational correlation. Although the average dislocation spacing (ξ_D) is similar to ξ_T, ξ_D is always larger than ξ_T at the smallest impurity concentration (Table I). The fact that $\xi_T < \xi_D$ in the x(Nb)=0.02 samples indicates that factors in

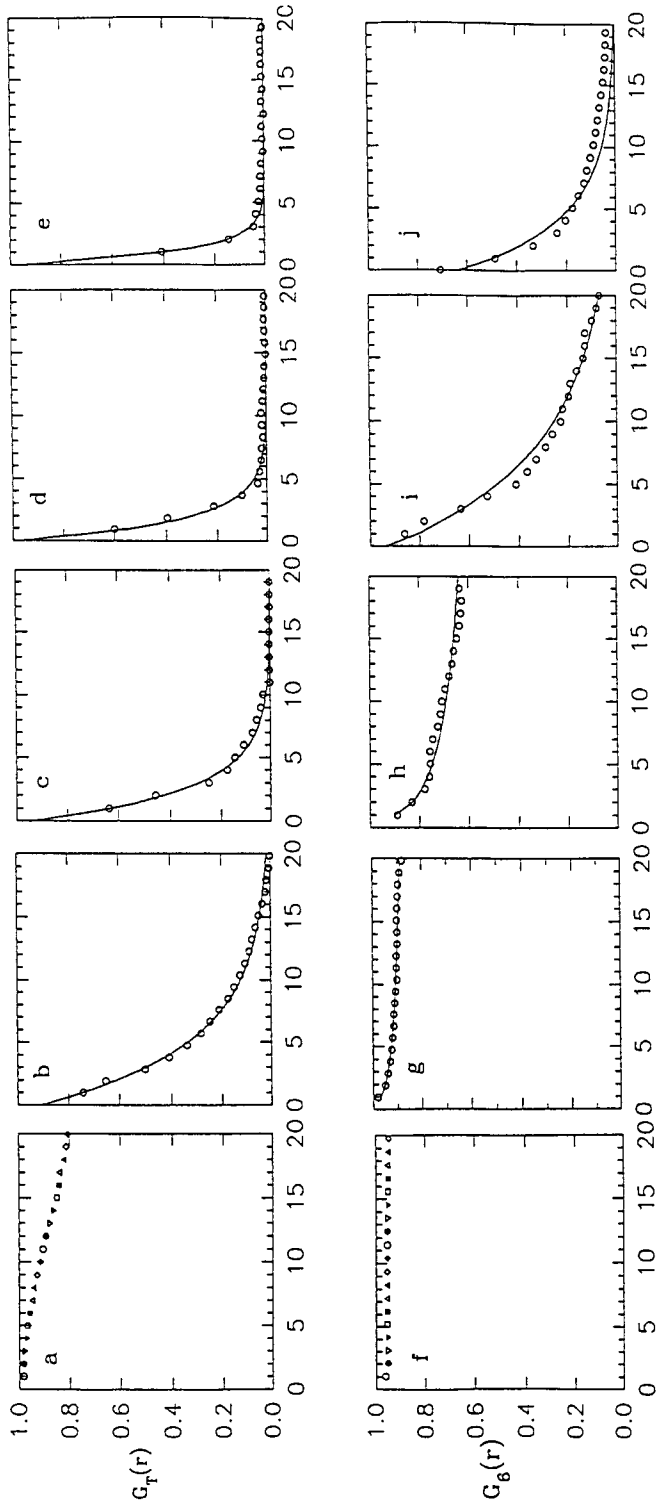

Fig. 17. Translational correlation functions $G_T(r)$ (a-e) for the x = 0, 0.02, 0.04, 0.07, and 0.10 $Nb_xTa_{1-x}S_2$ materials, respectively. Orientational correlation functions $G_6(r)$ (f-j) for x = 0, 0.02, 0.04, 0.07 and 0.10, respectively. The x-axes in these figures correspond to CDW lattice constants. The points represent the experimental data and the lines correspond to exponential fits, $\exp(-r/\xi)$, (a-e) and (i, j) or power law fits, $r^{-\eta}$, (g, h). Reproduced from Ref. 93.

addition to dislocations decrease translational order; this observation contrasts the prediction of equilibrium theory. However, we can explain this result (i.e., $\xi_T < \xi_D$) within the context of weak pinning theory. As discussed above, the CDW phase varies smoothly from $-\pi$ to π in regions separated by dislocations (i.e., within domains). The smooth variation in phase causes small distortions of the CDW lattice positions that reduce the translational order. Indeed, Chudnovsky has explicitly shown how elastic distortions (i.e., smooth variations in the phase vs. a singular phase variation at a dislocation) destroy the positional order of weakly pinned lattices [106]. Hence, a combination of the equilibrium melting and weak pinning theories provide a better description of the changes in translational correlation for this metal-substituted CDW system.

TABLE I.
Important length scales in the $Nb_xTa_{1-x}S_2$ CDW system.
(the units for d_i, ε_D, ε_T, ε_6 are CDW lattice constants)

$Nb_xTa_{1-x}S_2$	d_i	ε_D	ε_T	ε_6	η
x = 0.02	0.80	12	7 - 10	200	0.02
x = 0.04	0.57	8	3 - 6	100	0.13
x = 0.07	0.43	5	2 - 3	11	—
x = 0.10	0.36	3	1 - 2	5	—

4.3.4 Other Comments: Pinning and Dimensionality

The analysis discussed above indicates that the CDW state in $Nb_xTa_{1-x}S_2$ can be treated as a two-dimensional system. Because dimensionality plays an essential role in determining the physical properties of materials (e.g., the physics of critical phenomena), we examine further the consequences of the dimensionality of a system below.

The CDW pinning theory developed earlier shows that different effects should arise from pinning in systems of different dimensionality. First, domain formation should occur for a weakly pinned CDW for $d < 4$ [84,85,89]. This prediction for domain formation does not, however, lead to a distinguishable criteria in our system. Secondly, the impurity concentration dependence for pinning also varies significantly for systems of different dimensionality. This variation is readily apparent upon examination of the parameter ε in equation 9. For a 1D CDW chain, $\varepsilon \approx \rho_0 V_0/n_i\kappa \propto n_i^{-1}$. Hence, in a one-dimensional system, the pinning should be strong if the impurities are dilute and pinning should be weak if the impurities are dense. In 2D, however, $\varepsilon \approx \rho_0 V_0/\kappa$. This indicates that the pinning strength (weak or strong) should be independent of impurity concentration. Our studies are consistent with this prediction since the results for the $Nb_xTa_{1-x}S_2$ materials indicate that pinning is weak for $0 \leq x \leq 0.1$.

As indicated above, melting in 2D also differs fundamentally from melting in 3D. The solid to liquid phase transition in a 3D solid is an abrupt first order phase transition with discontinuities in the thermodynamic parameters. However, 2D melting is characterized by two continuous phase transitions that are mediated by topological defects. The first transition is from a crystalline solid to a hexatic phase and is caused by paired dislocations unbinding into isolated dislocations. The second transition is from the hexatic phase to a liquid phase and is caused by dislocation unbinding into isolated disclinations. Our investigations of the Nb-doped materials bear a strong resemblance to the theoretical predictions for 2D melting, and do not exhibit an abrupt phase transition based on our analysis of the structural order. However, these systems are clearly not ideal 2D systems and it is expected there is at least small 3D couplings (i.e., between layers). The effect of interlayer coupling has been considered theoretically by McMillan [87]. He argued that weak coupling of the CDW phase between layers will provide 3D stiffness to the CDW, and hence, it should not undergo a 2D melting transition. To clarify this issue, it will be necessary to assess experimentally the strength of the interlayer interactions and the 3D stiffness of the CDW. In the future these parameters could be probed by determining thermodynamic quantities (e.g., heat capacity) and the structure as a function of temperature.

A central result presented above is the direct elucidation of the structural manifestations of quenched impurity pinning. We have identified three different phases of the pinned IC CDW lattice, these are: (1) crystalline solid; (2) hexatic glass; and a (3) liquid-like state. It is interesting to ask whether there are observable consequences of these novel structural phases. Indeed, we find that these structurally distinct CDW states can be mapped to distinct macroscopic transport behavior. Resistivity data from the pure material exhibit a sharp first-order phase transition. However, in the hexatic glass regime (x(Nb) = 0.02 and 0.04) resistance versus temperature plots show a broadened phase transitions. Finally, in the liquid-like state (x(Nb) 0.07) no distinct transition is observed in the resistivity data. Thus, the three structurally distinct CDW phases may correspond to true thermodynamic phases. Other physical measurements, such as heat capacity and magnetic susceptibility, should also be carried out to confirm this suggestion.

5. New Directions: CDWs In Nanocrystals

It is widely recognized that Fermi surface nesting plays a vital role in CDW formation [56,75,77,86-88,107-112]. The Fermi surface of a nanocrystal can be modified by varying the size and shape of the crystal, and furthermore, for sufficiently small sizes the very concept of a Fermi surface will be ill-defined. As mentioned above, STM is an exciting tool for research on single nanoscale structures since it can in principle both create and probe the properties of very small structures. For example, STM has been used to manipulate individual atoms and molecules into structures [27,29,113-115], to probe quantum behavior in nanostructures 27,117], and to lithographically pattern surfaces [117-125].

Recently, we discovered a new approach to fabricate well defined nanocrystals on the surface of layered transition metal dichalcogenide [126]. We can create T phase $TaSe_2$ nanocrystals in the surface layer of 2H-$TaSe_2$ crystals by STM tip induced local solid-solid phase transition. Furthermore, it is possible to control the size of the T-phase $TaSe_2$ nanocrystals by varying the applied bias voltage during the tip-induced modification as shown in Figure 18. The three T-phase nanocrystals in these images have dimensions of 70, 35 and 7 nm. The two large nanocrystals (Figure 18a, b) exhibit relatively uniform commensurate CDW states. The CDW superlattice in both nanocrystals also show different domains that likely result from pinning to atomic lattice defects or the T/H-phase interface. In the smallest nanocrystal (Figure 18c), both the intensity and wavelength of the CDW are distorted relative to the uniform state observed in single crystals or the large nanocrystals. The CDW amplitude is larger at the center of the triangular nanocrystal, and furthermore, the wavelength appears to decrease from 12.5 Å at the center to 10.0 Å at the edge. We believe these results demonstrate that it is indeed possible to probe effects of size on the properties of a CDW state, although future systematic investigation will be needed to define the CDW physics in this new size regime.

6. Concluding Remarks

In this chapter, we have reviewed some of the recent advances in elucidating charge density wave structural and electronic properties in low dimensional metal chalcogenide compounds by scanning tunneling microscopy. Probing and understanding charge density waves in both pure and doped materials has been presented. In the one-dimensional pure $NbSe_3$ system, STM research has shown that all three atomic chains in this material are involved in forming the CDW phases at low temperature. In the two-dimensional 1T-TaS_2 compound, our STM studies have unambiguously identified the structure of the nearly-commensurate CDW state and thus resolved a long-standing problem. We have also shown how STM can be used to elucidate systematically CDW pinning and disorder with studies of $Nb_xTa_{1-x}S_2$ solids. Analyses of STM images demonstrate that Nb impurities introduce topological defects into the CDW lattice. Quantitative analysis of the density of dislocations and comparisons of this data with theoretical scaling arguments demonstrates that the pinning of the CDW by Nb impurities is in the weak-pinning regime. In addition, we have shown how pinning affects the translational and orientational order of the 2D CDW lattice. Calculations of the translational and orientational correlation functions suggest that the CDW lattice evolves continuously from a crystalline solid, $x(Nb) = 0$, to a hexatic glass, $0 < x(Nb) \leq 0.04$, and finally to an amorphous state, $x(Nb) \geq 0.07$. Finally, we have shown that the structural evolution of the CDW lattice with increasing impurity concentration has many analogous features to equilibrium melting in 2D, although there are differences that likely arise from the quenched disorder and pinning in $Nb_xTa_{1-x}S_2$. We believe that $M_xTa_{1-x}S_2$ materials will be ideal systems for future studies since

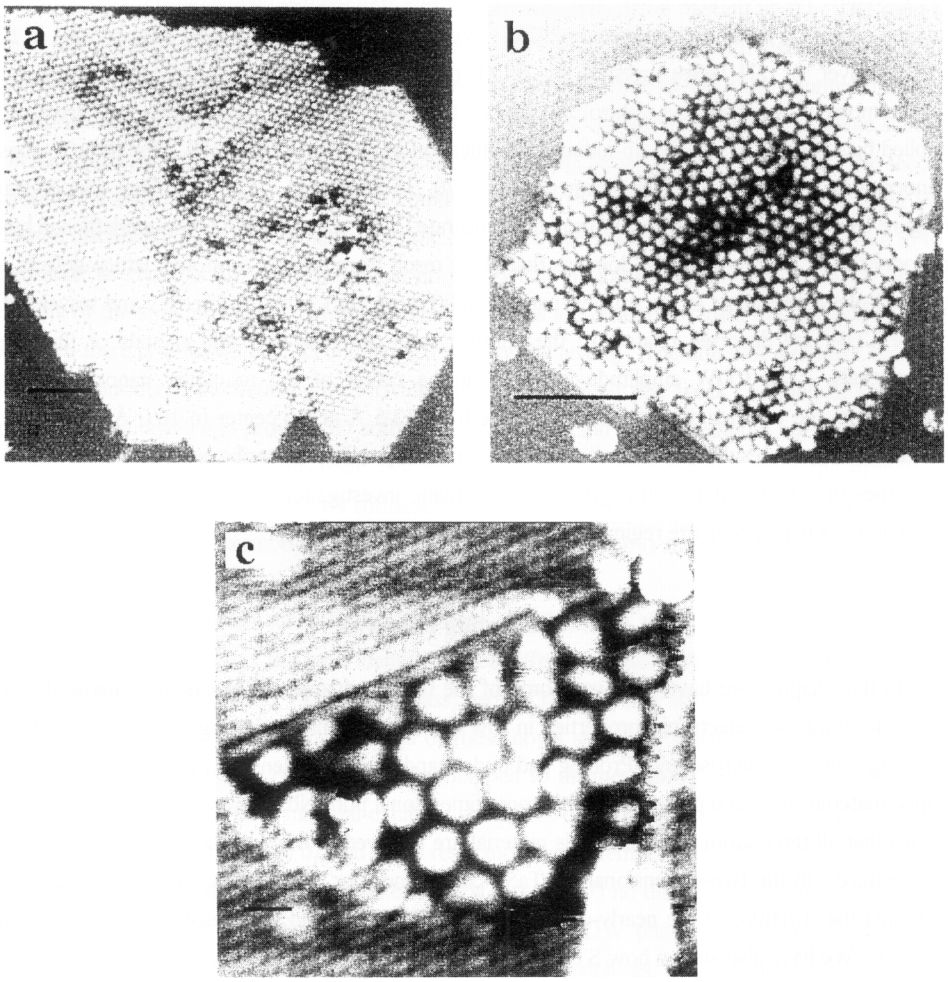

Fig. 18. STM images of T-phase nanocrystals that were created using different applied voltage. The T-phase nanocrystals in these images are all located near the center of the image frame. The nanocrystals in (a), (b) and (c) were made using voltages of -1400 mV, -1300 mV and -1200 mV respectively. The scale bar in (a), (b) and (c) are 10, 10 and 1 nm, respectively. Reproduced from Ref. 127.

the impurity concentration and potential can be varied systematically, and since the CDW-lattice coupling can be changed through variations in the temperature. Hence, experimental and theoretical investigations of this system will lead to a much deeper understanding of pinning and non-equilibrium disorder in 2D systems. In a more general sense, it is clear from this work that STM can provide key insight into understanding the microscopic properties of other complex low-dimensional solids [4]. Future investigations of such materials will undoubtedly lead to significant advances in our understanding of materials.

Acknowledgment

C.M.L. acknowledges support from the National Science Foundation (DMR-9306684), the Air Force Office of Scientific Research (AFOSR 94-1-0010) and the Materials Science and Engineering Center of the National Science Foundation (DMR-9400396).

References

1. G. Binnig, H. Rohrer, C. Gerber, and E. Weibel, *Phys. Rev. Lett.*, **49**, 57 (1982).
2. G. Binnig and H. Rohrer, *Sci. Am.*, *August*, 50 (1985).
3. C.F. Quate, *Phys. Today*, **39,** 26 (1986).
4. H.J. Guntherodt and R. Wiesendanger, Eds., *Scanning Tunneling Microscopy*, Springer-Verlag, Berlin, 1992.
5. C.J. Chen, *Introduction to Scanning Tunneling Microscopy*, Oxford University Press, New York, 1993.
6. P. K. Hansma and J. Tersoff, *J. Appl. Phys*, **61**, R1 (1987).
7. Y. Kuk and P. J. Silverman, *Rev. Sci. Instru.*, **60**, 165 (1989).
8. J. E. Griffith and G. P. Kochanski, *Annu. Rev. Mater. Sci.*, **20**, 194 (1990).
9. P. Avouris, *J. Phys. Chem.*, **94**, 2246 (1990).
10. R.V. Coleman, B. Giambattista, P.K. Hansma, A. Johnson, W.W. McNairy, and C.G. Slough, *Adv. Phys.*, **37**, 559 (1988).
11. C.M. Lieber, J. Liu, and P.E. Sheehan, *Angew. Chem. Int. Ed. Engl.*, **35**, 687 (1996).
12. C.M. Lieber, *C&EN News,* April 18, 28(1994).
13. X.L. Wu and C.M. Lieber, *Progress in Inorganic Chemistry*, S. J. Lippard, Ed., John Wiley & Sons, Inc, New York, 1991.
14. C.M. Lieber and X.L. Wu, *Acc. Chem. Res.*, **24**, 170 (1991).
15. H. Dai and C.M. Lieber, *Annu. Rev. Phys. Chem.*, **44**, 237 (1993).
16. Q. Zhong, D. Inniss, K. Kjoller, and V.B. Elings, *Surf. Sci. Lett.*, **290**, L688 (1993).
17. M.T. Beal-Monod, C. Bourbonnais, and V.J. Emery, *Phys. Rev. B*, **34**, 7716 (1986).
18. G. Binnig, C.F. Quate, and C. Gerber, *Phy. Rev. Lett.*, **56**, 930 (1986).
19. R.J. Colton and J.S. Murday, *Naval Res. Rev.*, **3**, 2 (1988).
20. P.K. Hansma, V.B. Elings, O. Marti, and C.E. Braker, *Science*, **242**, 209 (1988).
21. C.F. Quate, *Surface Science*, **299/300**, 980 (1994).
22. J.P. Spatz, S. Sheiko, M. Moller, R.G. Winkler, P. Reineker, and O. Marti, *Nanotechnology*, **6**, 40 (1995).
23. S. Yoon, H. Dai, J. Liu, and C.M. Lieber, *Science*, **265**, 215 (1994).
24. J. Frommer, *Angew. Chem. Int. Ed. Engl.*, **31**, 1298 (1992).
25. D. Rugar and P. Hansma, *Physics Today*, October, 23 (1990).
26. P.E. Sheehan and C.M. Lieber, *Science*, **272**, 1158 (1996).
27. M.F. Crommie, C.P. Lutz, and D.M. Eigler, *Science*, **262**, 218 (1993).
28. P. Avouris, *Acc. Chem. Res.*, **28**, 95 (1995).
29. J.A. Stroscio and D.M. Eigler, *Science*, **254**, 1319 (1991).
30. P. Avouris, *Acc. Chem. Res.*, **27**, 159 (1994).
31. J.C. Patrin and J.H. Weaver, *Phys. Rev. B*, **49**, 17913 (1993).
32. D. Rioux, R.J. Pechman, M. Chander, and J.H. Weaver, *Phys. Rev. B*, **50**, 4430 (1994).
33. K. Koguchi, T. Matsumoto, and T. Kawai, *Science*, **267**, 71 (1995).
34. M. Kanai, T. Kanai, K. Motui, X.D. Wang, T. Hashizume, and T. Sakurai, *Surface Science*, **326**, L619 (1995).
35. F.J. DiSalvo and T.M. Ricc, *Physics Today,* April, 23 (1979).
36. D.M. Ginsburg, *Physical Properties of High Temperature Superconductors*, World Scientific, Singapore, 1989.
37. H.F. Hess, *Methods of Experimental Physics*, Academic Press, Inc., New York, 1993.
38. H.F. Hess, R.B. Robinson, and J.V. Waszczak, *Phys. Rev. Lett.*, **64**, 2711 (1990).
39. H.F. Hess, R.B. Robinson, R.C. Dynes, J.M. Valles, and J.V. Waszczak, *Phys. Rev. Lett.*, **62**, 214 (1989).
40. G. Binnig and H. Rohrer, *Angew. Chem. Int. Ed. Engl.*, **26**, 606 (1987).
41. R.J. Hamers, *Annu. Rev. Phys. Chem.*, **40**, 351 (1989).

42. J. Tersoff and D.R. Hamann, *Phys. Rev. B.*, **31**, 805 (1985).
43. J. Tersoff, *Phys. Rev. B*, **41**, 1235 (1990).
44. N.D. Lang, *Phys. Rev. Lett.*, **56**, 1164 (1986).
45. A. Selloni, P. Caenevalli, P.E. Tosatti, and C.D. Chen, *Phys. Rev. B*, **33**, 5770 (1986).
46. C.J. Chen, *Phys. Rev. Lett.*, **65**, 448 (1990).
47. J. Bardeen, *Phys. Rev. Lett.*, **6**, 57 (1963).
48. S. Kagoshima, H. Nagasawa, and T. Sambongi, *One-Dimensional Conductors*, Springer-Verlag, New York, 1985.
49. R.E. Thorne, *Physics Today*, May, 42 (1996).
50. *Electronic Properties of Inorganic Quasi-One-Dimensional Compounds*, Ed. P. Monceau, Reidel, Boston, 1985.
51. *Low-Dimensional Electronic Properties of Molybdenum Bronzes and Oxides*, Ed. C. Schlenker, Kluwer, Dordrecht, 1989.
52. P. Monceau, N.P. Ong, and A.M. Portis, *Phys. Rev. Lett.*, **37**, 602 (1976).
53. N. Shima and H. Kamimura, *Theoretical Aspects of Band Structure and Electronic Properties of Pseudo-One-Dimensional Solids*, Reidel, Boston, 1985.
54. R.M. Fleming, D.E. Moncton, and D.B. McWhan, *Phys. Rev. B*, **18**, 5560 (1978).
55. G. Gruner, *Rev. Mod. Phys*, **60**, 1129 (1988).
56. J. McCarten, D.A. Dicarlo, M.P. Maher, T.L. Adelman, and R.E. Thorne, *Phys. Rev. B*, **46**, 4456 (1992).
57. G. Gruner and A. Zettl, *Phys. Rep.*, **119**, 117 (1985).
58. L.P. Gorkov and G. Gruner, *Charge-Density Waves in Solids*, North-Holland, Amsterdam, 1989.
59. D. Jerome, *Low-Dimensional Conductors and Superconductors*, Vol. 155, Plenum, 1987.
60. S. van Smaalen, J.L. DeBoer, P. Coppen, and H. Graafsma, *Phys. Rev. Lett.*, *67*, 1471 (1991).
61. S. van Smaalen, J.L. DeBoer, A. Meersma, H. Graafsma, H.S. Sheu, A. Darovskikh, and P. Coppens, *Phys. Rev. B*, **45**, 3103 (1992).
62. J.H. Ross, Z. Wang, and C.P. Schlichter, *Phys. Rev. Lett.*, **56**, 633 (1986).
63. Z. Dai, C.G. Slough, and R.V. Coleman, *Phys. Rev. Lett.*, **67**, 1472 (1991).
64. C.G. Slough, W.W. McNairy, R.V. Coleman, J. Garnaes, C.B. Prater, and P.K. Hansma, *Phys. Rev. B*, **42**, 9255 (1990).
65. C.G. Slough and R.V. Coleman, *Phys. Rev. B*, **40**, 8042 (1989).
66. C.G. Slough, B. Giambattista, A. Johnson, W.W. McNairy, and R.V. Coleman, *Phys. Rev. B*, **39**, 5496 (1989).
67. J. Ren and M. H. Whangbo, *Phys. Rev. B*, *46*, 4917 (1992).
68. R.M.A. Leith and J.C. Terhell, *Preparation and Crystal Growth of Materials with Layered Structures*, Reidel, Dordretch, 1977.
69. J.A. Wilson, F.J. DiSalvo, and S. Mahajan, *Adv. Phys.*, **24**, 117 (1975).
70. F.J. DiSalvo, J.A. Wilson, B.G. Bagley, and J.V. Waszczak, *Phys. Rev. B.*, **12**, 2220 (1975).
71. R.L. Withers and J.A. Wilson, *J. Phys. C: Solid State Phys.*, **19**, 4809 (1986).
72. K. Nakanishi, H. Takatera, Y. Yamada, and H. Shiba, *J. Phys. Soc. Jpn.*, **43**, 1509 (1977).
73. K. Nakanishi and H. Shiba, *J. Phys. Soc. Jpn.*, **43**, 1839 (1977).
74. R.V. Coleman, B. Drake, P.K. Hansma, and C.G. Slough, *Phys. Rev. Lett.*, **55**, 394 (1985).
75. X.L. Wu and C.M. Lieber, *Science*, **243**, 1703 (1989).
76. X.L. Wu and C.M. Lieber, *Phys. Rev. Lett.*, **64**, 1150 (1990).
77. R.E. Thomson, U. Walter, E. Ganz, J. Clark, and A. Zettle, *Phys. Rev. B.*, **38**, 10734 (1988).
78. B. Giambattista, C.G. Slough, W.W. McNairy, and R.V. Coleman, *Phys. Rev. B*, **41**, 10082 (1990).
79. F. J. DiSalvo, *Science*, **247**, 649 (1992).
80. *Physics Through 1990's: Condensed Matter Physics*, Natl. Acad. Press., Washington, 1986.
81. Z. Zhang, , Harvard University, 1993.
82. A.K. Cheetham and P. Day, *Solid State Chemistry: Techniques*, Clarendon, Oxford, 1987.
83. X.L. Wu, Y. Wang, Z. Zhang, J. Huang, and C.M. Lieber, *Science*, **248**, 1211 (1990).
84. H. Fukuyama and P.A. Lee, *Phys. Rev. B*, **17**, 535 (1978).
85. P.A. Lee and T.M. Rice, *Phys. Rev. B*, **19**, 3970 (1979).
86. H. Frohlich, *Proc. Roy. Soc. A.*, **223**, 296 (1954).
87. W.L. McMillan, *Phys. Rev. B.*, **12**, 1187 (1975).
88. H. Matsukawa and H. Takayama, *J. Phys. Soc. Japan*, **56**, 1507 (1987).
89. Y. Imry and S.-K. Ma, *Phys. Rev. Lett.*, **35**, 1399 (1975).
90. F.R.N. Nabarro, *Theory of Dislocations*, Dover, New York, 1967.

91. S.N. Coppersmith, *Phys. Rev. Lett.*, **65**, 1044 (1990).
92. H. Dai, H.-F. Chen, and C.M. Lieber, *Phys. Rev. Lett.*, **66**, 3183 (1991).
93. H. Dai and C.M. Lieber, *Phys. Rev. Lett.*, **69**, 1576 (1992).
94. D.R. Nelson, M. Rubinstein, and F. Spapen, *Philos. Mag. A.*, **46**, 105 (1982).
95. C.A. Murray, P.L. Gammel, D.J. Bishop, D. J. Mitzi, and A. Kapitulnik, *Phys. Rev. Lett.*, **64**, 2312 (1990).
96. R. Seshadri and R.M. Westervelt, *Phys. Rev. Lett.*, **66**, 2774 (1991).
97. S. Fortune, *Algorithmica*, **2**, 153 (1987).
98. G.F. Voronoi, *J. Reine Agnew. Math.*, **134**, 198 (1908).
99. C.A. Murray, W.O. Sprenger, and R.A. Wenk, *Phys. Rev. B.*, **42**, 688 (1990).
100. D.G. Grier, C.A. Murray, C.A. Bolle, P.L. Gammel, D.J. Bishop, D.B. Mitzi, and A. Kalpitulnik, *Phys. Rev. Lett.*, **66**, 2270 (1991).
101. N.D. Mermin, *Phys. Rev.*, **176**, 250 (1968).
102. R.E. Peierls, *Helv. Phys. Acta.*, 7, 81 (1923).
103. B.I. Halperin and D.R. Nelson, *Phys. Rev. Lett.*, **4**, 121 (1978).
104. D.R. Nelson and B.I. Halperin, *Phys. Rev. B.*, **19**, 2457 (1979).
105. S.-K. Ma, *Modern Theory of Critical Phenomena*, Benjamin/Cummings, Reading, 1976.
106. E.M. Chudnovsky, *Phys. Rev. B.*, **43**, 7873 (1991).
107. W.L. McMillan, *Phys. Rev. B.*, **14**, 1976 (1976).
108. L. F. Mattheiss, *Phys. Rev. B.*, **8**, 3719 (1973).
109. H.W. Myron and A.J. Freeman, *Phys. Rev. B*, **15**, 885 (1977).
110. A.W. Overhauser, *Phys. Rev.*, **128**, 1437 (1962).
111. A. W. Overhauser, *Phys. Rev.*, **167** (1968).
112. M.-H. Whangbo, R.J. Cava, F.J. DiSalvo, and R.M. Fleming, *Solid State Communications*, **43**, 277 (1982).
113. L.J. Whitman, J.A. Stroscio, R.A. Dragoset, and R.J. Celotta, *Science*, **251**, 1206 (1991).
114. I.-W. Lyo and P. Avouris, *Science*, **253**, 173 (1991).
115. T.A. Jung, R.R. Schlitter, J.K. Gimzewski, H. Tang, and C. Joachim, *Science*, **271**, 181 (1996).
116. P. Avouris and I.-W. Lyo, *Science*, **264**, 942 (1994).
117. S. Rubel, M. Trochet, E.E. Ehrichs, W.F. Smith, and A.L. d. Lozanne, *J. Vac. Sci. Technol. B*, **12**, 1894 (1994).
118. J. A. Dagata, *Science*, **270**, 1625 (1995).
119. E.A. Dobisz and C.R.K. Marrian, *Appl. Phys. Lett.*, **58**, 2526 (1991).
120. A.D. Kent, T.M. Shaw, S.V. Molar, and D.D. Awschalom, *Science*, **262**, 1249 (1993).
121. A. Zaluska, L. Zaluski, and A. Witek, *Mat. Sci. Eng., A*, **122**, 251 (1989).
122. U. Staufer, R. Wiesendanger, L. Eng, L. Rosenthaler, H.-R. Hidber, H.-J. Guntherodt, and N. Garcia, *J. Vac. Sci. Technol. A*, **6**, 537 (1988).
123. A. Sato and Y. Tsukamoto, *Nature*, **363**, 431 (1993).
124. A. Sato and Y. Tsukamoto, *Advanced Materials*, **6**, 79 (1994).
125. A. Sato, S. Momose, and Y. Tsukamoto, *J. Vac. Sci. Technol. B, Microelectron. Nanometer Struct.*, **13**, 2832 (1995).
126. J. Zhang, J. Liu, J. Huang, P. Kim and C.M. Lieber, *Science*, **274**, 757 (1996).